Global Empirical Picture of Magnetospheric Substorms Inferred from Multi-Mission Magnetometer Data

G. K. Stephens[1], M. I. Sitnov[1], H. Korth[1], N. A. Tsyganenko[2], S. Ohtani[1], M. Gkioulidou[1], A. Y. Ukhorskiy[1]

[1]The Johns Hopkins University Applied Physics Laboratory, 11100 Johns Hopkins Road, Laurel MD 20723-6099, USA.
[2]Institute and Department of Physics, Saint Petersburg State University, Saint Petersburg, Russia.

Corresponding author: Grant Stephens (Grant.Stephens@jhuapl.edu)

Key Points:

- Substorm tail current sheet thinning and dipolarization are reproduced using novel data mining technique
- Global 3-D structure of substorm currents including the substorm current wedge is reconstructed from data
- Substorms contribute to an accumulation of a longer-lived thick current in the innermost part of the magnetosphere

Abstract

Magnetospheric substorms represent key explosive processes in the interaction of the Earth's magnetosphere with the solar wind, and their understanding and modeling is critical for space weather forecasting. During substorms, the magnetic field on the night side is first stretched in the anti-sunward direction and then it rapidly contracts earthward bringing hot plasmas from the distant space regions into the inner magnetosphere, where they contribute to geomagnetic storms and Joule dissipation in the polar ionosphere, causing impressive splashes of aurora. Here we show for the first time, that mining millions of spaceborne magnetometer data records from multiple missions allows one to reconstruct the global 3-D picture of these stretching and dipolarization processes. Stretching results in the formation of a thin (less than the Earth's radius) and strong (up to ~6 nA/ m^2) current sheet, which is diverted into the ionosphere during dipolarization. In the meantime, the dipolarization signal propagates further into the inner magnetosphere resulting in the accumulation of a longer-lived current there (~2 nA/ m^2 with a total strength of ~2 MA), giving rise to a proto-geomagnetic storm. The global 3-D structure of the corresponding substorm currents including the substorm current wedge is reconstructed from data.

Plain Language Summary

Using several millions of historical magnetometer records and data mining techniques we form virtual spacecraft constellations of tens of thousands of spacecraft to reconstruct the global shape of the terrestrial magnetosphere at the moments of its most dramatic reconfigurations responsible for major space weather disturbances.

1 Introduction

The magnetic field generated by Earth's core creates a cocoon around our planet called the magnetosphere, which shields life from the hazardous flow of high-energy particles emanating from the Sun and carried via the solar wind (McComas et al., 2011). Magnetospheric plasmas are virtually collisionless, and as a result, the fundamental processes that govern their evolution, such as magnetic reconnection, may involve microscopic scales comparable to the electron gyroradius (Burch et al., 2016), which makes their global first-principle description difficult. At the same time, with the multiple missions that have explored our planet's neighborhood in the space era, an opportunity arises to create a comprehensive empirical description of the magnetosphere, and in particular its magnetic field (Tsyganenko, 2013). The empirical models combine general expansions of the magnetospheric current systems with physics-based constraints on the global shape of the magnetosphere and the localization of its main currents. So far, such an approach has been successful for one class of major disturbances, magnetic storms (Tsyganenko & Sitnov, 2007; Sitnov et al., 2008, 2010, 2018; Stephens et al., 2016). Storms occur when the interplanetary magnetic field (IMF) orients southward (anti-parallel to the dayside terrestrial magnetic field) and persists for many hours. The resulting reconnection between the IMF and the magnetospheric magnetic field directly drives magnetospheric convection enhancing the near-Earth "ring" current, which is observed using magnetometers on the surface of the Earth, from which the geomagnetic indices are calculated, such as the low-latitude *Sym-H* index (Iyemori, 1990). As a result, mining spacecraft magnetometer data with similar values of *Sym-H* and its trends allows one to reconstruct the storm picture (Sitnov et al., 2008, 2010, 2018; Stephens et al., 2016).

Unlike storms, substorms were first recognized due to their high-latitude auroral manifestations (Akasofu, 1964) and the corresponding magnetic field disturbances reflected by auroral indices such as the *AL* index (Davis & Sugiura, 1966). They represent another class of space weather phenomena associated with the global reconfiguration of the magnetosphere (Angelopoulos et al., 2008, 2013). Substorms are more transient and less predictable than storms and they may cause substantial damage to satellites (Connors et al., 2011) and ground-based systems (Boteler, 2001). They also inject the seed populations of energetic radiation belt particles that are further accelerated during storms (Reeves et al., 2003; Turner et al., 2015; Baker et al., 2016). Since the beginning of space era, substorms were considered as building blocks of storms (Chapman, 1962; Kamide, 1992; Kamide et al., 1998; Sharma et al. 2013). However, quantitative description of that substorm-to-storm assembling process has remained an unsolved problem for more than half a century.

Even after several recent multi-probe missions aimed to understand substorm mechanisms, such as THEMIS (Angelopoulos et al., 2008) and MMS (Burch et al., 2016), a global quantitative picture of the reconfiguration of the geomagnetic field and underlying electric currents is still missing. Several case studies with fortunate conjunctions of multiple probes (Sergeev, Angelopoulos, et al., 2011; Petrukovich et al., 2013; Artemyev et al., 2016) suggest that substorms often begin with a 30–50-minute period (termed the "growth" phase) where the nightside magnetic field stretches in the anti-sunward direction and the tail current sheet (CS) becomes strong (J ~10 nA/m^2) and thin, with the thickness of a fraction of the Earth radius R_E, comparable to the thermal ion gyroradius (Runov et al., 2006; Sergeev, Angelopoulos, et al., 2011). Moreover, the thinning process is multi-scale because the thin current sheet (TCS) forms inside of another, much thicker CS. Observations also suggest that during the most active and transient "expansion" phase, the stretched magnetic field becomes more dipolar, which is interpreted as an addition of a dawnward flowing equatorial current in the near-Earth magnetotail forming a part of a new current system, termed the "substorm current wedge" (SCW) (McPherron et al., 1973). It connects the tail CS with the ionosphere via earthward (downward) field-aligned currents (FACs) on the eastern side of the wedge and tailward (upward) FACs on the western side. This current system, is similar in sense to higher-latitude currents connecting the ionosphere with the distant parts of the magnetosphere and its boundaries, coined region-1 FACs (Iijima & Potemra, 1976) or R1. But it is opposite to the FACs (henceforth called R2) connecting the ionosphere with the westward storm-time current on the night side also known as the partial ring current or PRC (Fukushima & Kamide, 1973). Later, based on magnetohydrodynamic (MHD) simulations (Birn et al., 1999) and observations (Sergeev, Tsyganenko, et al., 2011; Sergeev et al., 2014) it was suggested that the structure of substorm current systems is more complex, and it also includes an additional R2-sense system. Whether the latter becomes a part of the PRC could not be resolved, because MHD models do not describe energy-dependent particle drifts that control storm currents. So far, the empirical reconstruction of substorms was limited to a number of custom-tailored descriptions of the corresponding current systems, such as ad hoc TCS models of the growth phase (Pulkkinen et al., 1991; Kubyshkina et al., 1999) and wire-type SCW models (Tsyganenko, 1997, Sergeev, Tsyganenko, et al., 2011; Sergeev et al., 2014). Thus, the global structure of substorm currents, which is key for understanding their mechanisms (Angelopoulos et al., 2008, 2013), remained a mystery.

Below we present results of an empirical reconstruction of the substorm current systems covering all key phases of this phenomenon within the same data-analysis framework, based on the largest ever set of Earth magnetospheric magnetometer data, a detailed description of currents, and advanced data mining algorithms. For the first time, we infer from data the global structure and evolution of key substorm elements, the TCS and SCW, as well as a part of the ring current accumulated after each substorm that persists in time lengths nearing storm-scales.

The following section describes the basic methodology of the empirical reconstruction of the substorm magnetic field, including the model structure, data mining procedure, database, fitting, and optimization details. In section 3 we present the main results of the reconstruction, including thinning and dipolarization of the magnetotail, the evolution of the TCS and complementary thick CS, the 3-D SCW, as well as storm-scale currents associated with thick CS. The results are summarized and further discussed in section 4.

2 Empirical reconstruction of the geomagnetic field

The complexity of substorms along with the large volumes of data accumulated during the space era has motivated us to model substorms by mining data within a system science approach (Vassiliadis, 2006), in which their global description, characterized by the *Sym-H* and *AL* indices, is used to bin the database of spacecraft magnetic field measurements. The different stages of substorm evolution, such as the growth and recovery phases, is reflected in the time derivatives of these indices. To capture the spatial structure of the magnetic field, an empirical model is employed, whose coefficients are adjusted by fitting the model to data.

A fundamental tradeoff when developing an empirical model is balancing model complexity with data availability. For instance, a model with too many degrees of freedom will be subject to overfitting, whereas an underfit model will not fully capture the breadth of information contained in the data. With this tradeoff in mind, a new class of empirical magnetic field models was developed (Tsyganenko and Sitnov, 2007, Sitnov et al., 2008) (henceforth termed the TS07D model). The idea was to develop a malleable (as opposed to rigid and hand-tailored) model and dynamically bin and fit a subset of the measured magnetic field vectors from the database (as opposed to having one universal fit of the model, each moment in time is binned and fit separately), thus enabling the reconstruction of the dynamics of the magnetosphere be dictated by the data.

Below, we first report the model architecture followed by the description of the magnetometer database. After this, the dynamical data mining technique is detailed. In particular, we will demonstrate how the architecture and data mining have been upgraded to allow for empirical reconstruction of substorm current systems and their dynamics.

2.1 Model Architecture

The total magnetic field as measured by spacecraft within the magnetosphere, can be decomposed into two primary components, the field due to the Earth itself (internal), and the field created by electric currents flowing in space (external): $\mathbf{B}_{tot} = \mathbf{B}_{int.} + \mathbf{B}_{ext.}$ The most commonly used internal field model in the space physics community is the IGRF model (Thébault et al., 2015), and in the context of this work is assumed to be perfectly accurate. The goal here is to model the external field. It is further decomposed into different constituents owing to the primary magnetospheric current systems, in this model the equatorial, field aligned, and magnetopause currents $\mathbf{B}_{ext.} = \mathbf{B}_{eq.} + \mathbf{B}_{FAC} + \mathbf{B}_{MP}$.

2.1.1 Equatorial Field Description

The description of the equatorial currents follows the formulation originally developed for the TS07D empirical magnetic field model (Tsyganenko & Sitnov, 2007; Sitnov et al., 2008). This model diverged from earlier models, where the approach is to describe each equatorial current system (symmetric ring current, partial ring current, and tail current) individually using a predefined analytical description. In TS07D, these individual modules are replaced by an expansion of orthogonal basis functions.

$$\mathbf{B}^{(eq)}(\rho,\phi,z;D)=\sum_{n=1}^{N}a_n^{(s)}\mathbf{B}_n^{(s)}+\sum_{m=1}^{M}\sum_{n=1}^{N}\left(a_{mn}^{(o)}\mathbf{B}_{mn}^{(o)}+a_{mn}^{(e)}\mathbf{B}_{mn}^{(e)}\right)\#(1)$$

The form of these functions comes about as the magnetic vector potential solution to Laplace's equation for a thin current sheet, i.e. given $\mathbf{j}^{(eq)}(\rho,\phi,z)=\left(j_\rho\hat{\boldsymbol{\rho}}+j_\phi\hat{\boldsymbol{\phi}}\right)\delta(z)$ derive $\mathbf{A}(\rho,\phi,z)$. Using separation of variables, the solution ends up using a combination of sines and cosines for the azimuthal dependence, Bessel functions for the radial dependence, and an exponential decay function for the *Z*-dependence. The magnetic field components can be computed by taking the curl of the magnetic vector potential solution. This procedure ensures a divergenceless magnetic field. To introduce a thickness to the current sheet, the *Z*-coordinate is replaced with $\zeta=\sqrt{z^2+D^2}$. This broadens the delta profile in height and introduces a characteristic half-thickness parameter D.

During the substorm growth phase, a thin current sheet (TCS) develops within the thicker magnetotail plasma current sheet (CS), resulting in a magnetotail with two different characteristic half-thicknesses. To describe such a configuration, the idea was simply to double the aforedescribed solution:

$$\mathbf{B}^{(eq)}(\rho,\phi,z)=\mathbf{B}^{(eq)}(\rho,\phi,z;D)+\mathbf{B}^{(eq)}(\rho,\phi,z;D_{TCS})\#(2)$$

In this expansion the thickness of the main (presumably thick) CS can be arbitrary and it is only restricted by the data-fitting procedure, while the TCS thickness has an ad hoc upper limit $D_{TCS} < D_0$, which is taken to be equal to 2 R_E in view of observations (Runov et al., 2006; Sergeev, Angelopoulos, et al., 2011) showing that D_{TCS} is of the order of the thermal ion gyroradius, that is, $D_{TCS} < 2R_E$.

The solar wind compresses the magnetosphere, and its dynamic pressure ($P_{dyn}=\rho V^2$) has long been known to correlate with the magnitude of the equatorial magnetic field (Siscoe et al., 1968). The first effect is directly built into the model in the construction of the magnetopause currents (described below). The latter is accounted for by representing each expansion coefficient as a binomial $a_{mn}\rightarrow a_{mn,0}+a_{mn,1}\sqrt{P_{dyn}}$, where the square root of the dynamic pressure was chosen as the functional dependence.

The magnetotail orients its configuration along the Sun-Earth line motivating the use of the Geocentric Solar Magnetospheric (GSM) coordinate system. However, closer to the Earth, where the field is still approximately dipolar, the field aligns with the dipole axis, prompting the use of the Solar Magnetic (SM) coordinate system (Laundal & Richmond, 2017). These two coordinates differ by a single Euler angle rotation, which has been termed the dipole tilt angle. Thus, to model the magnetic field and the associated magnetospheric current systems, they must transition from one to the other. This is accomplished by formulating the current systems assuming no dipole tilt as described above and then applying the deformation technique formulated in (Tsyganenko, 1998). This reflects the hinging of the magnetotail, as well as its warping and twisting, as described in detail in (Tsyganenko, 1998, 2002). The corresponding hinging, warping, and twisting coefficients are free parameters of the model to be obtained from the data-fitting procedure. We note, these deformations warp the magnetic equator so that it no longer lies in a plane. This can make direct comparisons between different times complex, as both the current systems and their dipole tilt deformations change with time. For this reason, when plotting the 2-D equatorial panels in equatorial and 3 D distributions described below, the deformation has been turned off by setting the hinging, warping, and twisting effects to zero. This also aligns the magnetic equator with the equatorial plane.

2.1.2 Field Aligned Currents

The cartoon representation of the FACs describes them as two concentric dawn-dusk antisymmetric conical currents flowing into and out of Earth, where the higher and lower latitude systems have been termed R1 and R2 respectively. The actual structure inferred from data is much more complex even during quiet times (Iijima & Potemra, 1976) and especially during substorms (Zou et al., 2009; Murphy et al., 2013). In particular, the Harang discontinuity (Harang, 1946) and the SCW, require higher order descriptions to effectively model them. Thus, this substorm model utilizes the more flexible FAC module detailed in (Sitnov et al., 2017). The local time (azimuthal) dependence of the current density is determined using the first four terms of a Fourier series, where the amplitude coefficients are determined when the model is fit to magnetometer data. It is noted that the first term ($A\sin(\phi)$) corresponds to the primary dawn-dusk antisymmetry, while the second term ($B\cos(\phi)$) introduces a rotation as seen by the trigonometric relation: $A\sin(\phi) + B\cos(\phi) = \sqrt{A^2 + B^2}\sin(\phi + \Delta\phi)$. The second two terms are higher order modes and allow for finer scale local time structure.

$$j(\phi) = A\sin(\phi) + B\cos(\phi) + C\sin(2\phi) + D\cos(2\phi) \#(3)$$

The latitudinal dependence is determined by solving the magnetic vector potential representation of a thin conical current sheet: $\nabla^2\mathbf{A} = -\mu_0\mathbf{J}$ using separation of variables. The solution is of the form $A_r(\phi,\theta) = \sum_{m=1}^{N} B_m T^{(m)} \sin m\phi$. The functions $T^{(m)}$ were found in (Tsyganenko, 1991). However, this solution is rather rigid, so a linear combination of these modules can be used while still being a solution to the above equation. Two such modules are used for both FAC regions that half overlap. The result is a total of sixteen linear coefficients (four azimuthal multiplied by four latitudinal) that determine the FAC structure, which is capable of reconstructing the Harang discontinuity.

To this point, the FACs are described as cones emanating from the origin, so a deformation is applied that bends the current sheets along approximately dipolar field lines. An additional deformation accounts for the day-night asymmetry, the dipole tilt angle, and a global rescaling of the FAC system (Tsyganenko, 2002). The global rescaling parameter allows the FAC currents to shift to different latitudes and introduces two additional free non-linear parameters (for R1 and R2) that are fit as described below.

2.1.3 Magnetopause Currents

Each magnetospheric current system in the empirical description has its supplementary magnetopause (so-called Chapman-Ferraro) current system, which minimizes the internal magnetic field outside the magnetopause (Tsyganenko & Sitnov, 2007). The model assumes a closed magnetosphere, i.e. the magnetic field does not penetrate the magnetopause. This is accomplished by adding to each of the above fields and the Earth's internal field a complementary shielding field $\mathbf{B}_{sh}$, which satisfies the condition $(\mathbf{B}+\mathbf{B}_{sh})\cdot\boldsymbol{n}|_s = 0$, where the surface is the modeled magnetopause. The general idea is based on the fact that the magnetopause currents do not penetrate inside the magnetosphere. Hence, their magnetic field is curl free there and can be derived as a solution of Laplace's equation $\nabla^2 U = 0$. The general solution can be found from separation of variables and becomes a linear expansion in the chosen coordinate system. The coefficients of this linear expansion can be solved by sampling the magnetopause surface and then minimizing the r.m.s. normal component of the total field. The magnetopause boundary is represented by an analytical function whose form was shown in (Tsyganenko, 1995). This functional form was fit to the empirically derived magnetopause computed in (Shue et al., 1998).

For example, each equatorial expansion was shielded with a cylindrical harmonic expansion, see eq. 20 of (Tsyganenko & Sitnov, 2007). The Earth's internal field is a bit more complicated, owing to the strong dependence of the dipole tilt. This is solved by splitting the scalar potential U into two independent scalar potentials for the portions of the field parallel and perpendicular to the *X*-axis: $U = U_\parallel \sin\Psi + U_\perp \cos\Psi$, where the solution for $U_\parallel$ and $U_\perp$ are solved using Cartesian coordinates. The FAC is shielded using a similar combination of Cartesian solutions, except owing to the even more complicated structure, additional terms are necessary to reduce the residuals (eq. 34 of (Tsyganenko, 1995)). Finally, the changes in the solar wind dynamic pressure cause the magnetopause to expand and contract in a self-similar way (Shue et al., 1998). This effect can be replicated in the shielding currents by scaling the position by $\mathbf{r}'(P_{dyn}) = \left(\frac{P_{dyn}}{P_{dyn,0}}\right)^{\epsilon}\mathbf{r}$. Here ϵ is taken to be 0.155 based on the analysis in (Shue et al., 1998).

2.2 Data Mining Procedure

To mine magnetometer records for magnetic field reconstruction, which are most relevant to the moment of interest we employ the nearest-neighbor (NN) approach (Mitchell, 1997; Vassiliadis, 2006; Wu et al., 2008; Sitnov et al., 2008, 2012). In this approach, the global state of the magnetosphere is filled with data records that fall into a small number of M global parameters. These are either derived from geomagnetic indices that reflect specific phases of magnetic storms and substorms or from solar wind measurements that act as a driver of the magnetospheric dynamics. Then a subset of the historical database to be used to reconstruct the magnetic field is determined as a small vicinity around the query point in the M-dimensional space of global parameters.

Geomagnetic indices were developed to measure different aspects of geomagnetic activity. In this study, the *Sym-H* and *AL* indices are utilized as they are widely considered to be metrics of storm and substorm activity respectively (Rostoker, 1972). During storms, charged particles become trapped in orbits that encircle the Earth, leading to a predominantly westward flowing symmetric ring current. Magnetometers situated at low and mid-latitudes on the surface of the Earth observe this current as a magnetic field that is opposite in direction of the main dipole field (called the horizontal component or *H*). The *Sym-H* index (Iyemori, 1990) averages six *H*-component measurements from mid-latitude magnetometer stations at 1-minute cadence. It is analogous with the 1-hour cadence *Dst* index (Rostoker, 1972). However, the magnetopause currents also significantly impact the value of the magnetic field at the surface of the Earth (Burton et al., 1975). To account for this, the 'pressure-corrected' index is computed to remove the contributions from the magnetopause currents: $Sym\text{-}H^{*} = A \cdot Sym\text{-}H - B \cdot \left(P_{dyn}\right)^{1/2}$, where the values of A and B are taken to be 0.8 and 13.0 respectively (Tsyganenko, 1996). During the substorm expansion phase, a westward substorm electrojet forms in the ionosphere, which translates into a decrease in the observed *H*-component in magnetometers located along the auroral zone in the northern hemisphere. Then the *AL* index is derived as the lower envelope of these geomagnetic variations at selected (10–13) observatories along the auroral zone. Since the substorm electrojet is the dominant ionospheric current during the expansion phase, the *AL* index reflects the level of substorm activity. More discussions on the use of *AL* and other geomagnetic indices in the global characterization of substorms can be found in (Rostoker, 1972; Partamies et al., 2013; McPherron & Chu, 2017).

Solar wind quantities have also long been known to correlate with geomagnetic activity (Newell et al., 2007, and references therein). Of particular interest is the value of vB_{south}^{IMF}. Here $-v$ is the *X*-component of the solar wind bulk flow velocity in the GSM coordinate system and B_{south}^{IMF} is the southward component of the IMF ($B_{south}^{IMF} = -B_{z}^{IMF}$ when $B_{z}^{IMF} < 0$ and $B_{south}^{IMF} = 0$ otherwise). The quantity vB_{south}^{IMF} has been shown to be the major driver of storms (Burton et al., 1975) and highly correlated with substorms (Blanchard & McPherron, 1995).

The storm state of the magnetosphere is determined by smoothing the pressure-corrected *Sym-H* index using a weighted moving average where the weights are defined by a half-cosine window function (Sitnov et al., 2012)

$$G_1(t) = \langle Sym\text{-}H^{*}|(t) \propto \int_{-\Pi/2}^{0} Sym\text{-}H^{*}(t+\tau)\cos(\pi\tau/\Pi)d\tau \ \#(4)$$

and its smoothed time derivative is defined as

$$G_2(t) = D\langle Sym\text{-}H^{*}|/Dt \propto \int_{-\Pi/2}^{0} Sym\text{-}H^{*}(t+\tau)\sin(2\pi\tau/\Pi)d\tau \ \#(5)$$

which is necessary, in particular, to distinguish between the main and recovery storm phases. The averaging constant $\Pi=\Pi_{st}$=12 hours (Sitnov et al., 2008) is chosen to eliminate the effects on shorter (e.g., substorm) time scales. The notation $\langle ...|$ is used to indicate that the window function only averages over past data, which prevents the smoothed parameter from being influenced by future data, and the notation $D\langle ...|/Dt$ to reflect that it is not equal to the true time derivative.

Similarly, the substorm state of the magnetosphere is determined by the smoothed *AL* index

$$G_3(t) = \langle AL| \propto \int_{-\Pi/2}^{0} AL(t+\tau)\cos(\pi\tau/\Pi)d\tau \ \#(6)$$

and its smoothed time derivative

$$G_4(t) = D\langle AL|/Dt \propto \int_{-\Pi/2}^{0} AL(t+\tau)\sin(2\pi\tau/\Pi)d\tau \ \#(7)$$

which should distinguish between the growth, expansion, and recovery phases of substorms. The corresponding averaging time scale is now $\Pi=\Pi_{sst}$=2.0 hours reflecting the typical duration of a substorm (Partamies et al., 2013).

To take into account the solar wind and IMF input we introduce a fifth global parameter

$$G_5(t) = \langle vB_{south}^{IMF}| \propto \int_0^{\tau_\infty} vB_{south}^{IMF}(t - \tau_\infty + \tau)\exp[(\tau - \tau_\infty)/\tau_0]d\tau \#(8)$$

with an e-folding time of τ_0=0.5 hours, based on the duration of a typical substorm growth phase (Partamies et al., 2013). The integration limit is τ_∞=6τ corresponding to six e-foldings. Thus, the dimension of the binning space is M=5. Smoothing the parameters serves to eliminate higher frequency oscillations that may be caused by noise and magnetospheric structures on time-scales smaller than substorm time-scales.

Then the NN vicinity of the query point $\mathbf{G}^{(q)}=\{G_1^{(q)},\ldots G_5^{(q)}\}$ is determined by the distance R= | $\mathbf{G}^{(i)}$- $\mathbf{G}^{(q)}$| of the NN points $\mathbf{G}^{(i)}$, i=1, … K_{NN}, in the 5-dimensional Euclidean space with the metric:

$$R = \left(\sum_{j=1}^{M} \delta_j \left(\frac{G_j}{\sigma_{G_j}}\right)^2\right)^{\frac{1}{2}} \#(9)$$

where σ_{G_j} is the standard deviation of the component G_j (additional factors δ_j are implemented to balance statistical weights of storm and substorm parameters; for example, putting them zero for G_1 and G_2 excludes storm effects from the binning procedure). In this study, all dimensions are weighted equally, i.e. δ_j=1. The number K_{NN} is chosen to have a sufficiently dense distribution of measurements for the reconstruction of the spatial structure of the geomagnetic field. On the other hand, it should be much less than the whole size K_{DB} of the model database to provide a sufficient selectivity of the NN method (for example, to distinguish between main and recovery phases of storms). The number of NNs used so far was $K_{NN} \sim 10^4 << K_{DB}$. Thus, the binning procedure based on the NN-approach represents a reasonable trade-off between past statistical models with $K_{NN} = K_{DB}$ (Tsyganenko & Sitnov, 2005, and refs. therein) and event-oriented models with $K_{NN} \sim 1$ (Kubyshkina et al., 1999).

The source of the geomagnetic indices and solar wind data are the 5-minute cadence datafiles from the OMNI database (https://omniweb.gsfc.nasa.gov/ow_min.html). As such, the cadence of the magnetic field reconstructions presented below is also 5-minutes.

2.3 Magnetometer Database

The original TS07D model was comprised of data from the Geotail, Cluster, Polar, Geostationary Operational Environmental Satellite (GOES) 8, 9, 10, and 12, and the Interplanetary Monitoring Platform (IMP) 8 missions (Tsyganenko & Sitnov, 2007). This set was chosen as it matches the beginning of continuous solar wind monitoring with the launch of the WIND spacecraft in late 1994 and included data through 2005. However, in the decade since that database was developed, Geotail, Cluster, and GOES continued to operate, and new missions launched, including five Time History of Events and Macroscale Interactions during Substorms (THEMIS) probes and the pair of Van Allen Probes spacecraft.

In constructing the new database, Cluster (2001–2016) and Polar (1996–2006) were reprocessed and included the newly collected data. In the original database, the four Cluster spacecraft were averaged into a single data source, but in the new reprocessing, they were treated as individual spacecraft. IMP-8, Geotail, and GOES 8, 9, 10, and 12 were left unchanged, even though some of them do have additional data. Incorporating these new data will take place in the future. The five THEMIS probes, launched in 2007, whose primary science objective is to resolve the timing, dynamics, and spatial scales of substorms, provided an extremely valuable set of magnetometer data in the magnetotail. In 2010, two of the THEMIS probes, began to change their orbit eventually becoming Lunar orbiters, thereby becoming the ARTEMIS mission. To filter out the transition period, the THEMIS data was filtered to exclude data for $r > 31\ R_E$, which matches the largest apogee of the THEMIS mission and the primary apogee of the Geotail mission. This filter was also applied to the IMP-8 and Geotail datasets, as occasionally, the sparse amount of data beyond 31 R_E, results in anomalous results, presumed to be caused by overfitting or Gibbs phenomena. The twin Van Allen Probe spacecraft, launched in 2012, have a perigee of a few hundred kilometers and an apogee of 5.8 R_E, and thus its data populate the equatorial inner-magnetosphere region that was missing in the original database.

Of the original set, only Polar and Cluster had perigees closer than Geosynchronous orbit, and only Polar had a perigee below 4 R_E. However, due to the large magnitude of the total field, there was a concern that small attitude errors would make it difficult to distinguish between the external and internal field and Polar data below 3.2 R_E were filtered. This concern was found to be overly conservative for equatorial spacecraft, as long as special attention was given to remove anomalous data points, and the new lower bound was changed to 1.5 R_E for equatorial spacecraft (Van Allen Probes and THEMIS). However, the 3.2 R_E was maintained for polar orbiting spacecraft (Polar and Cluster), not because of the attitude concern, but rather because of the large magnitude of the deviation in the field for the low-altitude FACs.

The magnetometer database is summarized in Table 1 (K_{DB} = 3,589,288). It is also described and available on the Space Physics Data Facility at the following URL: https://spdf.sci.gsfc.nasa.gov/pub/data/aaa_special-purpose-datasets/empirical-magnetic-field-modeling-database-with-TS07D-coefficients/. This study represents the first application of this new database.

Table 1.

Magnetospheric data of the extended set proposed as a basis of this study.

Spacecraft	Number	Period
Cluster 1	288,550	2001—2015
Cluster 2	289,725	2001—2015
Cluster 3	286,787	2001—2015
Cluster 4	225,048	2001—2015
Geotail	131,409	1994—2005
Polar	358,227	1996—2006
Imp8	3,160	1995—2000
Goes-08	233,674	1995—2003
Goes-09	84,951	1995—1998
Goes-10	213,295	1999—2005
Goes-12	79,569	2003—2005
Themis-A	286,382	2008—2015
Themis-B	26,580	2008—2010
Themis-C	42,863	2008—2010
Themis-D	286,592	2008—2015
Themis-E	290,104	2008—2015
Van Allen A	231,965	2012—2016
Van Allen B	230,407	2012—2016

2.4 Fitting the Model and Optimizing its Resolution

Now that the model has been formulated and the appropriate magnetometer data selected, the next step is to use the data to choose the value of the model's parameters. The model contains both linear coefficients and non-linear parameters. The first are found using the standard singular value decomposition method for linear regression (Press et al., 1992), the latter, including the scaling parameters of the FAC system, hinging, warping and twisting effects of the tail CS, as well as its thickness parameters D and D_{TCS}, are adjusted using the standard Nelder-Mead downhill simplex method, as described in more detail in (Press et al., 1992).

Additionally, another complication is that the spatial density of the data is largely non-uniform, potentially biasing the fit toward regions of the magnetosphere with a higher density of magnetometer data points, such as geosynchronous orbit, where the GOES satellites are located. A weighting scheme (Tsyganenko & Sitnov, 2007) is used that lowers/raises the weights in high/low density regions. The data is binned by $0.5\ R_E$ radial bins, e.g. one bin is the spherical shell consisting of $5.0\ R_E \leq r < 5.5\ R_E$. Each spacecraft contained in the bin is assigned a weight, $w_i = \frac{\langle \Delta N \rangle}{\max\left(\frac{\langle N \rangle}{5}, \Delta N_i\right)} \frac{\langle B \rangle}{\langle B_i \rangle}$. The first part is inversely proportional to the number of data points per bin (ΔN_i). The max function caps the maximum weight by preventing extremely underpopulated bins from getting a huge weight. The second part is inversely proportional to the average field of the points in that bin. This gives higher weights to bins (such as in the tail) where the external magnetic field is relatively small, and in unweighted least squares regression would have little impact in the target function. Together, these two factors help give the tail more influence in the fit than it would otherwise have in unweighted least squares regression.

There are several model configuration parameters that can be adjusted. Important are the number of equatorial expansions and the number of NNs to be used. In all previous iterations of the model reported in the literature (Tsyganenko & Sitnov, 2007; Sitnov et al., 2008, 2010, 2018; Sitnov, Stephens, et al., 2017; Stephens et al., 2013, 2016), the number of NNs was set to K_{NN}=8,000. This number was rather arbitrarily chosen by assuming that approximate size of the modeled magnetosphere is $20\ R_E \times 20\ R_E \times 20\ R_E = 8{,}000\ {R_E}^3$, so approximately one NN per cubic Earth Radii. Related to this is the number of azimuthal and radial expansions used in modeling the equatorial currents. Adding more expansions increases the potential resolution, but if the data density is too low, it risks introducing unphysical artifacts from overfitting or Gibbs phenomena. The original expansions were set to (M,N)=(4,5). The model was later customized by incorporating spacecraft data from the inner magnetosphere (Stephens et al., 2016), allowing for an increase in the number of expansions (M,N)=(6,20), but the analysis in the study was limited to $r \leq 7\ R_E$.

In this study, the original choice of K_{NN} was revisited. Choosing the number of NNs is a tradeoff. A smaller number of NNs (K_{NN}~1), leans the fitting towards event-oriented modeling, while a large number tends to statistical averaging. Specifically, a challenge here arose in that there is a significant decrease in the number of magnetic field measurements beyond $r \sim 12\ R_E$, which was the apogee for some of the THEMIS spacecraft for the most part of the mission. In the model validation presented in below Figure 1, the configuration matched that of (Stephens et al., 2016), as the THEMIS-E spacecraft's apogee was 12 R_E, thus enabling a higher resolution. But, in order to effectively describe the morphology throughout most of the inner magnetotail, i.e. when $r \leq 20\ R_E$, changes were made to eliminate overfitting in $12\ R_E \leq r \leq 20\ R_E$. First, the number of NNs was increased fourfold (8,000 to 32,000), and the number of expansions in the equatorial expansion was decreased to ((M,N)=(6,8)). The magnetotail reconstructions presented throughout the rest of the study use this configuration, with the exception of the comparison of THEMIS-E magnetometer data with the original and new substorm models presented in Figure 1. Here, the density of data located within $r \leq 12\ R_E$ allows for a greater number of expansions (M,N)=(6,20) with less NNs K_{NN} = 8,000.

3 Structure and evolution of substorm current systems

3.1 Thinning and dipolarization reproduced with the new data mining approach and compared with in situ observations

Figure 1 demonstrates the results of the model application (configured using K_{NN} = 8,000 and (M,N)=(6,20)) to a large group of substorms during the March 2008 magnetic storm. The comparison of the substorm model (red lines) with the baseline storm model TS07D (blue lines) shows that, unlike the latter, the new model captures the increase of the magnetic field $|B_x|$ measured by the THEMIS-E probe (black lines) that is responsible for the stretching of the magnetic field in the growth phase (Figure 1a). Also, it reproduces substorm dipolarization signatures seen as sharp positive spikes of the B_z field (Figure 1c) correlated with the dips of the *AL* index (Figure 1f). Thus, one can expect that the new model will reproduce the main substorm current systems and their evolution.

For this study, the first point in time prior to the substorm with a southward solar wind ($B_z^{IMF} < 0$) defines the start of the growth phase (dashed vertical red line). Substorm onset time (dashed vertical yellow line), i.e. the start of the expansion phase, is determined from the substorm onset time lists derived from the *SML* index (Newell & Gjerloev, 2011a, 2011b; Gjerloev, 2012) and the *MPB* index (McPherron & Chu, 2017). However, these two lists often differed substantially or entirely missed substorms observed from visual inspection of the *AL* index. For these cases, the onset times are determined by inspection of the SuperMag ground magnetometer vector plots. The start of the recovery phase is defined as the minimum of the *AL* index denoted by the dashed vertical blue line and the end of the recovery phase is defined when the *AL* index either returns to the baseline level (*AL* > -25 nT) or the next growth phase begins.

The definition of storm phases described above may differ from other substorm definitions, and in particular, the original notion of the auroral substorm (Akasofu, 1964), as discussed, for example in (McPherron, 2016, and refs. Therein). Here we use it mainly to place the discussion of our results into the context of the already known history of substorm studies. The definition of substorm phases does not affect in any way our data mining and fitting procedures. On the other hand, one can expect that the output of the present study can be used to improve the definitions of substorm phases and to make them more consistent.

The reconstruction accuracy of thinning and dipolarization processes shown in Figure 1 is reduced in the midst of the storms, near the *Sym-H* minimum (DOY=69–69.5). The most likely reason of this reduction is the significant effects of storm variations expressed by the *Sym-H* index in the data mining process, which extends now over the whole 5-D space equations (4)–(8) where the distribution of data with the selected K_{NN} becomes relatively scarce. However, away from the *Sym-H* minimum, the use of storm parameters in the binning space is important because it allows to separate substorms with different levels of the storm background, and in particular, to separate between storm-time and non-storm-time substorms.

Figure 2 shows another example of validation using the lower spatial resolution in the equatorial plane (M,N)=(6,8), and at the same time, the larger number of NNs in the binning sets

K_{NN} = 32,000. In spite of the fact that such changes worsen the validation results (they reduce B_z dipolarization peaks; thinning in this case is hard to evaluate because the probes are located relatively close to the plasma sheet), they allow for the use of more virtual probes for the spatial reconstruction to reveal the generic picture of substorms, which is discussed in the next section. Figure 2 still clearly shows that the new method reproduces dipolarizations observed by THEMIS probes A, D, and E (panels (b), (k), and (n)). Validation results for GOES-10 and GOES-12 shown in panels (p)–(r) and (v)–(x) suggest that the new empirical reconstruction works well at geosynchronous orbit, although the TS07D model does track B_z more accurately. This may not be entirely unexpected, as the TS07D database was comprised of a larger percentage of GOES data and only included storm-time parameters in the binning procedure. At the same time, panels (s) and (t) reveal substantial differences with GOES-11 data particularly during the second dipolarization. The reconstruction of B_z is reasonable during the growth phase but is underestimated during the expansion and recovery phases. In regards to THEMIS-B and THEMIS-C, these spacecraft map to $r > 20\ R_E$ for much of this interval and particularly for the second substorm, as can be seen in Figures S1–S3. Because these spacecraft were in this configuration for only about two years before becoming the Acceleration, Reconnection, Turbulence and Electrodynamics of the Moon's Interaction with the Sun (ARTEMIS) mission there is a lack of data in this region. As described above, the model resolution and K_{NN} number were chosen to optimize reconstruction in the region $r \leq 20\ R_E$, thus these spacecraft are largely beyond the range that the model is expected to perform optimally.

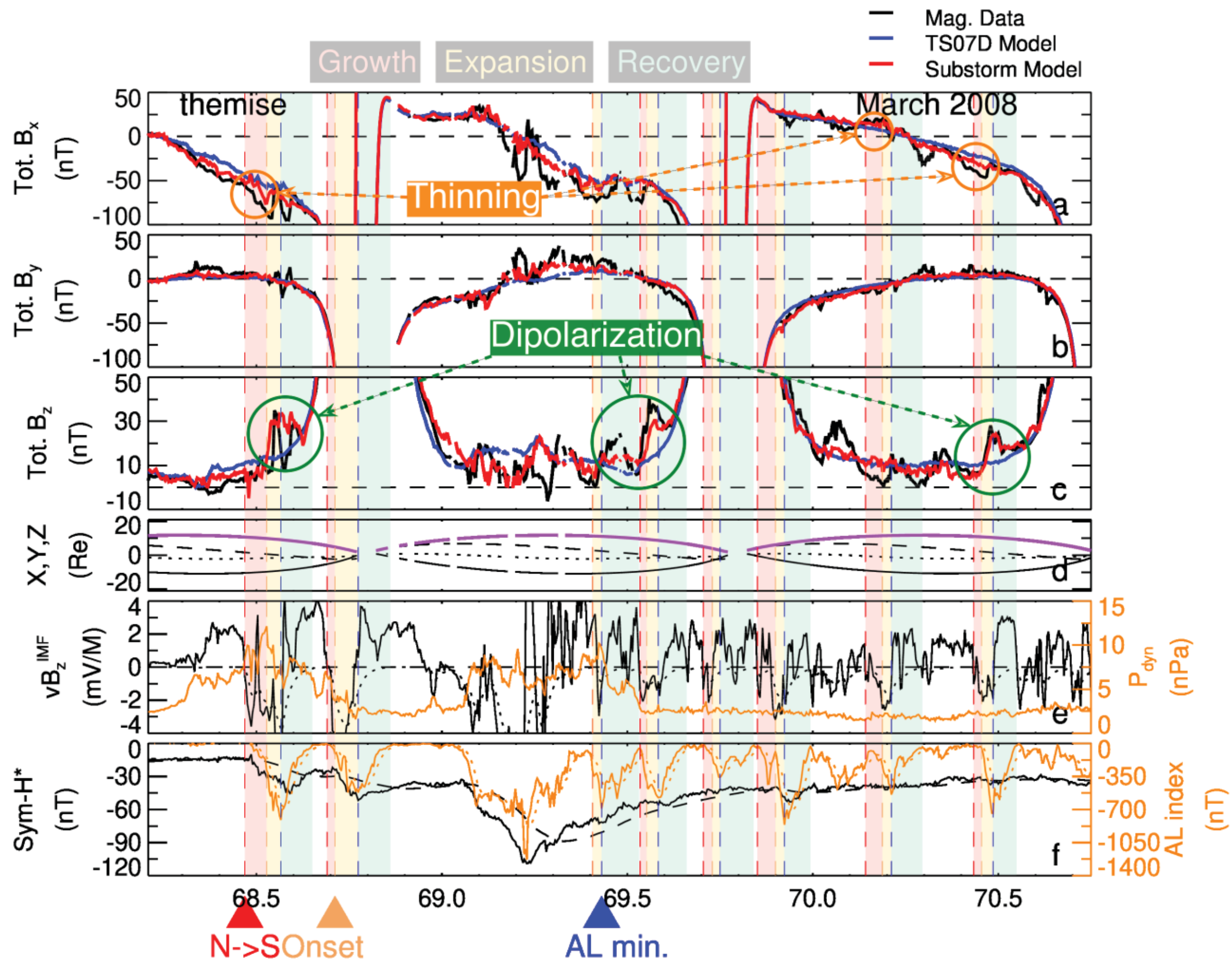

Figure 1. Key substorm signatures captured by the new data mining technique using a fleet of ~11,000 virtual spacecraft. Comparison of THEMIS-E magnetometer data with the original and new substorm data mining technique for a group of substorms during March 2008 magnetic storm. (a, b, and c) The *X*, *Y*, and *Z* components of the in situ magnetic field measured by the THEMIS-E magnetometer (black line) compared with the model evaluated at the spacecraft location, showing the original version of the model (blue line, configured with (M,N)=(6,8) and K_{NN} = 32,000) and the newly constructed substorm version of the model (red line, configured with (M,N)=(6,20) and K_{NN} = 8,000). The coordinate system used throughout this paper is GSM. (d) The ephemeris of the THEMIS spacecraft where the *X*, *Y*, *Z*, and *R* components correspond to the solid, dashed, dotted, and purple lines respectively. (e) Solar wind measurements; the electric field parameter vB_z^{IMF} and the smoothed vB_s^{IMF} parameter in solid and dotted black respectively, and the dynamic pressure in orange. (f) Geomagnetic indices; the pressure-corrected storm index (*Sym-H**) and its smoothed value in solid and dashed black respectively, and the substorm index (*AL*) and its smoothed value in solid and dotted orange respectively. The time cadence for these panels and for all subsequent plots is 5-minutes.

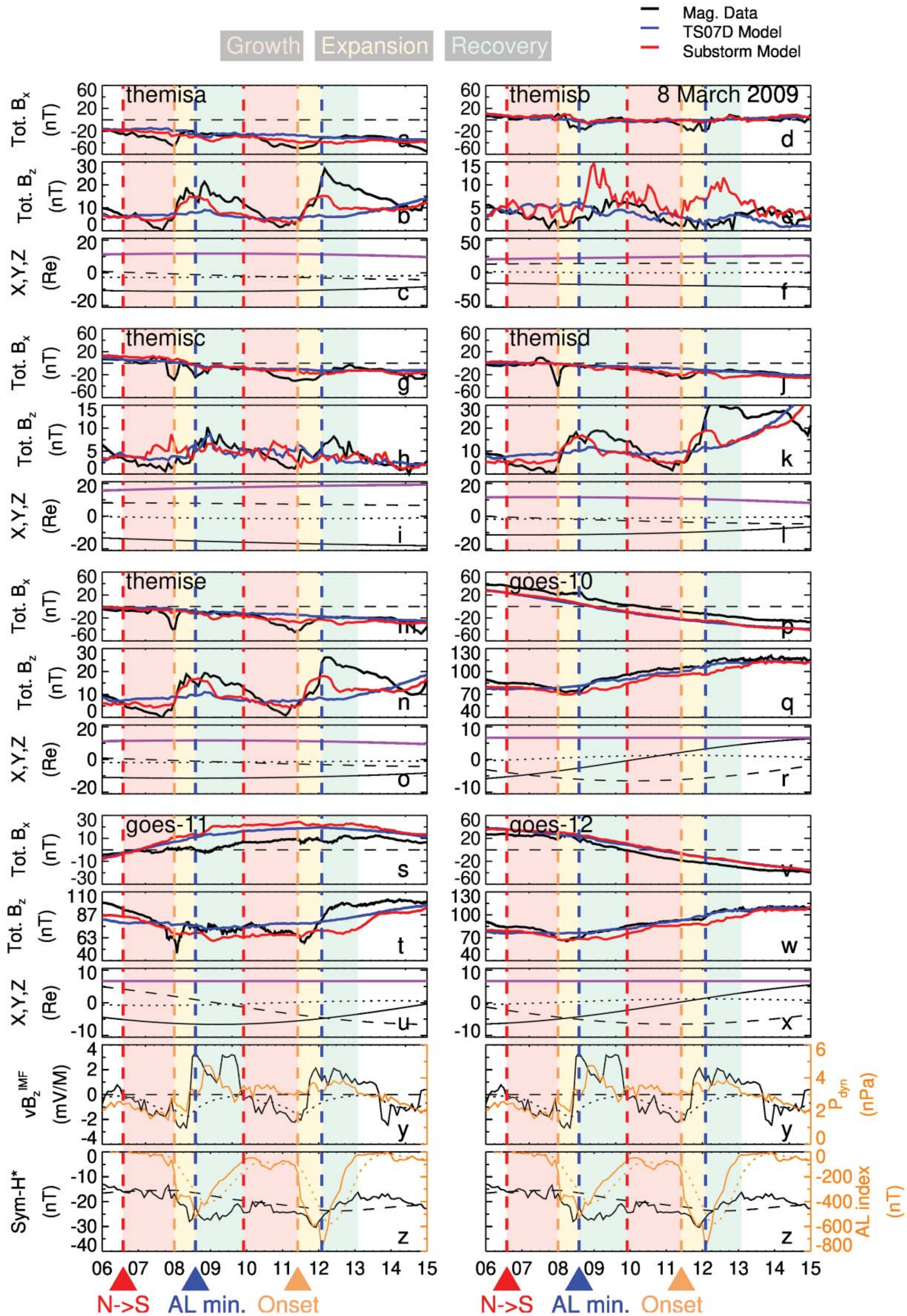
Mag. Data
TS07D Model
Substorm Model
Growth
Expansion
Recovery
themisa
themisb
8 March 2009
themisc
themisd
themise
goes-10
goes-11
goes-12
Tot. B_x (nT)
Tot. B_z (nT)
X,Y,Z (Re)
vB_z^{IMF} (mV/M)
P_{dyn} (nPa)
Sym-H* (nT)
AL index (nT)
N->S
AL min.
Onset

497

Figure 2. Comparison of THEMIS and GOES magnetometer data with the original and new substorm data mining technique for the March 8, 2009 substorms. (a and b) The X and Z components of the in situ magnetic field measured by the THEMIS-A magnetometer (black line) compared with the model evaluated at the spacecraft location, showing the original version of the model (blue line, configured with (M,N)=(6,8) and K_{NN} = 32,000) and the newly constructed substorm version of the model (red line, configured with (M,N)=(6,8) and K_{NN} = 32,000). (c) The ephemeris of the THEMIS spacecraft where the X, Y, Z, and R components correspond to the solid, dashed, dotted, and purple lines respectively. (d–x) Matches a, b, and c, except for the four other THEMIS spacecraft and the three GOES spacecraft. (y and z) Solar wind measurements and Geomagnetic indices respectively; similar to panels (e) and (f) in Figure 1 respectively. Note that in this run, compared to the set of March 2008 substorms shown in Figure 1, the following parameters have been changed to avoid overfitting in the key region 12 $R_E \leq r \leq 20$ R_E: K_{NN} was increased fourfold (8,000 to 32,000), and the number of expansions in the equatorial expansion was decreased ((M,N)=(6,8)).

3.2 Global distributions of the magnetic field and current in different substorm phases

We now focus on the reconstructions of a pair of non-storm substorms, which occurred on 8 March 2009. The substorm (marked by the AL dip in Figure 3a) started after an hour of the solar wind loading with $vB_z^{(IMF)}< 0$ (Figure 3b). Its late growth phase is characterized by formation of a deep (~4 nT) minimum of the B_z field (Figure 3d), which was derived recently from particle precipitation characteristics (Sergeev et al., 2018), and a large and strong (~6 nA/m^2) TCS providing a stretched tail configuration (Figure 3e). Figures 3f and 3g show the height integrated current density from the thick CS and the TCS part, respectively. It is seen that while the TCS occupies the broad local time region outside geosynchronous orbit (r ~6.6 R_E) and inside r ~15 R_E, the thick CS is located closer to Earth and in a wider local time region, including the day side sector. While the traditional picture of magnetospheric currents treats the ring current and tail current as spatially separated, however, Figure 3f and 3g shows that they form a single system, whose artificial separation in ad hoc models was rather misleading. The low-altitude FAC distribution in Figure 3c has the expected spiral pattern.

In the expansion phase, marked by the rapid decrease of the AL index in Figure 4a, the B_z minimum is replaced by a flux pileup region (Figure 4d), while the TCS disappears (Figure 4g) or even changes its direction to dawnward, resulting in the bifurcated structure of the meridional CS distribution near the neutral plane (Figure 4e, X≈-5 R_E), and providing a substantial dipolarization of the tail magnetic field highlighted by colored field lines. The 70° field line, that was open during the growth phase, is now closed indicating a shrinking of the polar cap boundary on the ionosphere. At the same time, the thick CS becomes greatly enhanced, particularly in the region $4\ R_E \leq r \leq 12\ R_E$ (Figure 4f) occupying a ~70° sector centered about local midnight. The comparison of Figure 4c with Figure 3c reveals strong enhancement of the FAC system (both R1 and R2-sense currents), particularly equatorward of the 70° latitude.

In the recovery phase (Figure 5), when the AL index increases approaching its base zero level (Figure 5a), the B_z field remains enhanced on the night side (Figure 5d) in spite of the rebuilding of the TCS (Figures 5e and 5g). The most interesting new feature in the empirical picture of this phase is the persistence of a strong thick CS penetrating deeply inside the geosynchronous region (Figure 5f).

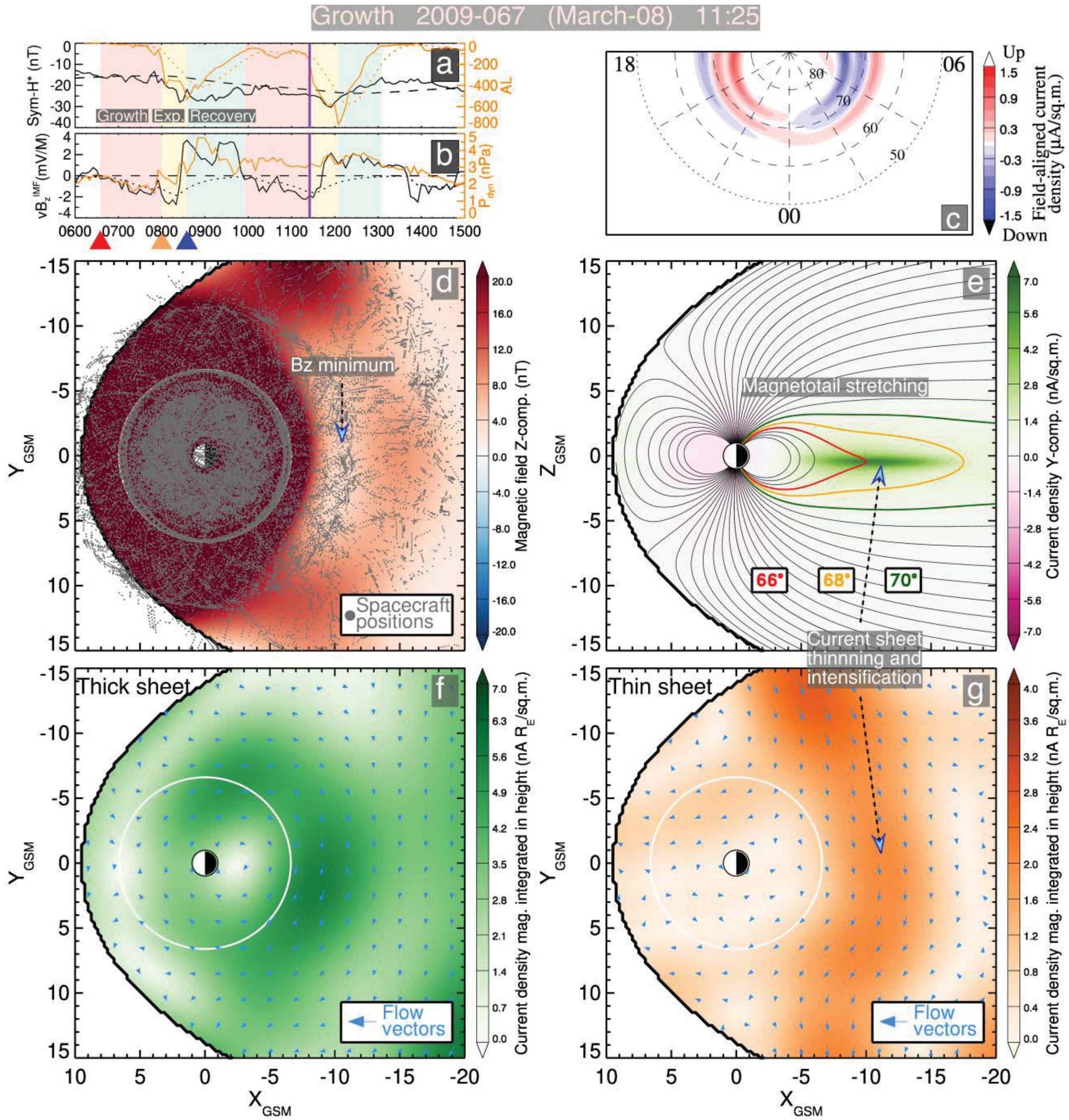

Figure 3. Reconstruction of the late growth phase of the March 8, 2009 substorm. Configured with (M,N)=(6,8) and K_{NN} = 32,000 corresponding to ~$5{\cdot}10^4$ virtual spacecraft (a and b) Geomagnetic indices and solar wind measurements respectively; similar to panels (f) and (e) in Figure 1 respectively. The vertical purple lines represent the moment in time. (c) The FACs flowing into and out of the ionosphere in blue and red respectively. (d) The equatorial slice of the total magnetic field with grey circles overplotted representing the locations of the magnetometers used to fit this moment. For the equatorial plots, the magnetic equator is forced to be coincident with this plane by setting the twisting and warping terms in the model zero. (e) The meridional slice of the *Y*-component of the current density, green indicates current flowing out of the page and purple into the page. Magnetic field lines are overplotted and start from the ionosphere at 60º with 2º step in latitude and with three of the field lines being highlighted. (f and g) The equatorial slice of the height integrated magnitude of the current density for the thick current sheet (CS) and thin current sheet (TCS) respectively (thick CS is integrated over $0 \leq Z \leq 5\ R_E$ and TCS is

integrated over $0 \leq Z \leq 1\ R_E$) with arrows overplotted showing the direction and magnitude of the current density vectors.

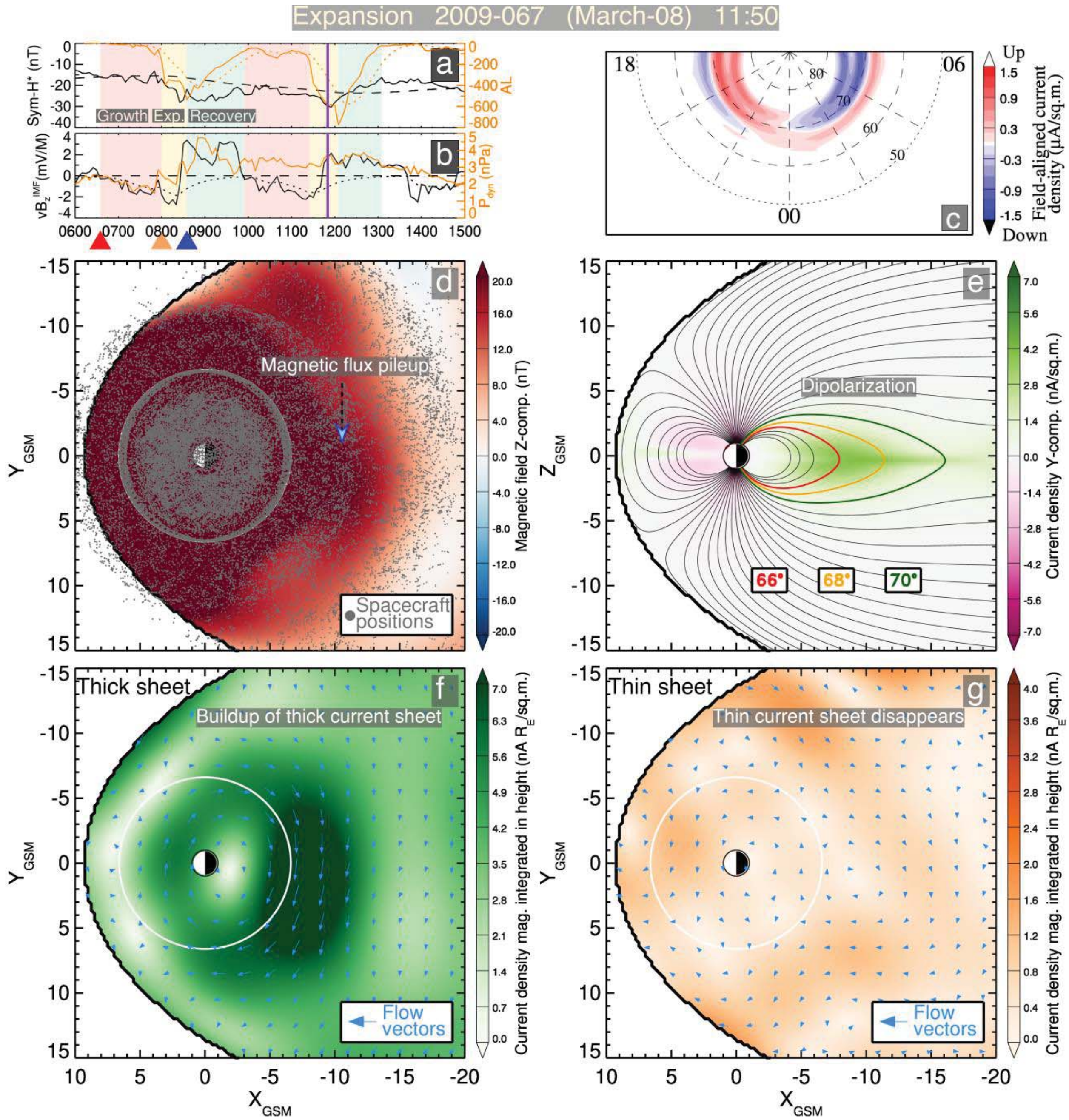

Figure 4. Reconstruction of the expansion phase of the March 8, 2009 substorm, featuring dipolarization of the nightside field lines (panels (d) and (e)), disappearance of the TCS (panels (e) and (g)) and the thick CS buildup (panel (f)). The panels are the same as in Figure 3 but except for a different moment in time.

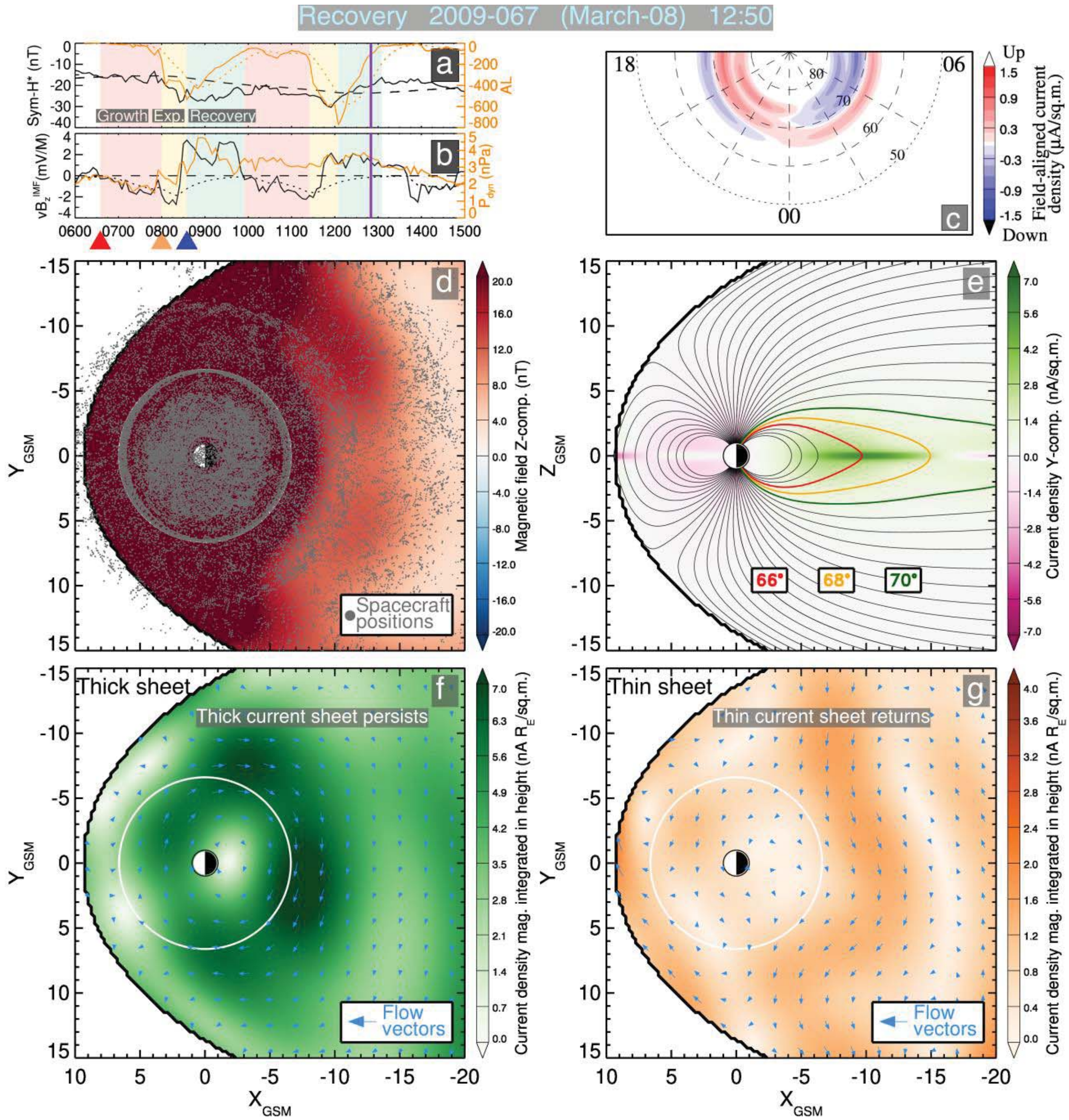

Figure 5. Reconstruction of the recovery phase of the March 8, 2009 substorm. Featuring the return of the TCS (panels (e) and (g)) and persistence of the thick CS (panel (f)). The panels are the same as in Figure 3 but except for a different moment in time.

3.3 Quantitative analysis of substorm currents and magnetic field variations

Further analysis of the March 2009 substorms presented in Figure 6 reveals the enhancement of all FAC components in both substorms (Figures 6c and 6d). They show the square roots of the sum of the squared amplitude coefficients $\left(\sum_{m=1}^{N} C_m{}^2\right)^{1/2}$ for the eight higher latitude and eight lower latitude modules. It should be noted that they are labeled as R1 and R2 based solely on their latitude. Since the modules overlap in latitude and possesses higher order modes, which of the coefficients contribute to the sense of the R1 and R2 current flow remains to be further investigated. The comparison between Figures 6c and 6d shows that while both R1 and R2 components are enhanced after the onset, the low-latitude R2 components dominate in the expansion phase. The corresponding equatorward shift of the FAC system is seen from the comparison of Figures 3c and 4c and is consistent with the results of in situ observations of substorm FACs using the Active Magnetosphere and Planetary Electrodynamics Response Experiment (AMPERE) and from ground-based magnetometer and optical instrumentation from the Canadian Array for Realtime Investigations of Magnetic Activity (CARISMA), as well as from THEMIS magnetometer arrays reported by Murphy et al. (2013).

These FAC amplitude variations anti-correlate with the evolution of the thick CS thickness (dark green line in Figure 6e). The evolution of the strength of the TCS and thick CS is plotted in Figure 6f. The thick CS resembles the conventional ring current (Figures 3f –5f), meanwhile the TCS contributes mainly to the magnetotail current (Figures 3g –5g). The strength of the TCS in Figure 6 is quantified as the amount of cross tail current flowing in the magnetotail and is computed by integrating the westward-flowing current density using a rectangular area integral: $I^{(thin)} = \int_{-1}^{+1}\int_{-16}^{-6} j_y^{(thin)}\, dxdz$. Only the TCS module is activated during this computation and dipole tilt effects are ignored by setting it to zero. Meanwhile, the thick CS current is instead computed by evaluating the integral on the noon meridian from the surface of the Earth to Geosynchronous orbit $I^{(thick)} = \int_{-5}^{+5}\int_{+1}^{+GEO} j_y^{(thick)}\, dxdz$, and is thus a measure of the conventional ring current.

According to Figures 6f and 6g, the most rapidly varying parameters are the TCS current and the equatorial magnetic field B_z. The TCS current gradually increases during the growth phase (from $I \approx 0.8$ MA to $I \approx 1.3$ MA for the second substorm) and then rapidly decreases during the expansion phase, even reaching negative values indicating an eastward TCS and reducing the total current, which results in the bifurcated current structure mentioned above, as confirmed by in situ multi-probe analysis (e.g. Fig. 4II in (Runov et al., 2006)). Meanwhile, B_z rapidly increases (from ~4 nT to ~21 nT for the second substorm) in the expansion phase after the preceding gradual decrease (from ~10 nT to ~4 nT) in the growth phase, in agreement with fortuitous in situ multi-probe observations (Sergeev, Angelopoulos, et al., 2011). The corresponding profiles in the growth and expansion phases, presented in two insets in Figure 6, show the magnetic field stretching and dipolarization over the whole tail, thus providing key information, which cannot be obtained in the foreseeable future by any real constellation mission (e.g., Petrukovich et al., 2013; Ohtani and Motoba, 2017).

Meanwhile the thick CS evolution (Figure 6f) proceeds on longer time scales. Its magnitude starts increasing during the expansion phase and stays enhanced at least an hour into the recovery phase. The time scales and radial location of the thick CS suggest that it describes the seed ring current responsible for storm dynamics of the magnetosphere. This hypothesis is supported by another group of substorms in the March 2008 storm (Figure 7). In particular, Figure 7f shows that the thick CS magnitude elevates during the first substorm in the March 2008 storm series and then remains elevated throughout the whole storm. We conclude that, in contrast to the TCS, which is an inherently substorm feature, the complementary thick CS should rather be characterized as a "proto-ring current" describing the contribution of substorms to the buildup of geomagnetic storms.

Other interesting features of the March 2008 main and early recovery phase (DOY=69–69.5) substorms (as seen in Figure 7) are overall elevated FAC amplitudes, which exceed their non-storm values (Figure 7c and 7d), and a strong dipolarization (B_z increase) at $\boldsymbol{r}$ = (-10.5 R_E, 0, 0) accompanied by a reduction of B_z in the inner magnetosphere near the Van Allen Probes apogee ($\boldsymbol{r}$ = (-5.8 R_E, 0, 0)) representing most likely combined substorm and storm effects. At the same time, according to Figure 7h, the substorm in the recovery phase of this storm reveals the same formation of the B_z hump at $X\approx$-16 R_E and the tailward B_z gradient earthward of it in the late growth phase of the substorm, which was seen for the March 8, 2009 substorm (Figures 3d and 6h). The formation of regions with a tailward B_z gradient has recently been recognized as a key feature of magnetotail destabilization mechanisms, including tearing (Sitnov & Schindler, 2010; Merkin et al., 2015; Merkin & Sitnov, 2016; Sitnov, Merkin, et al., 2017; Birn et al., 2018), ballooning/interchange (Pritchett and Coroniti, 2013), and flapping (Erkaev et al., 2007) instabilities. Thus, the new data mining approach advances earlier multi-probe measurements (Petrukovich et al., 2013; Ohtani and Motoba, 2017) and machine-learning analysis (Yue et al., 2015), because it resolves the tailward B_z gradient effect. Note that this finding is consistent with the earlier statistical studies (Wang et al., 2004, Fig. 9b) and the statistical visualization of substorms (Machida et al., Fig. 2c), as well as the most recent results obtained by remote sensing methods (Sergeev et al., 2018).

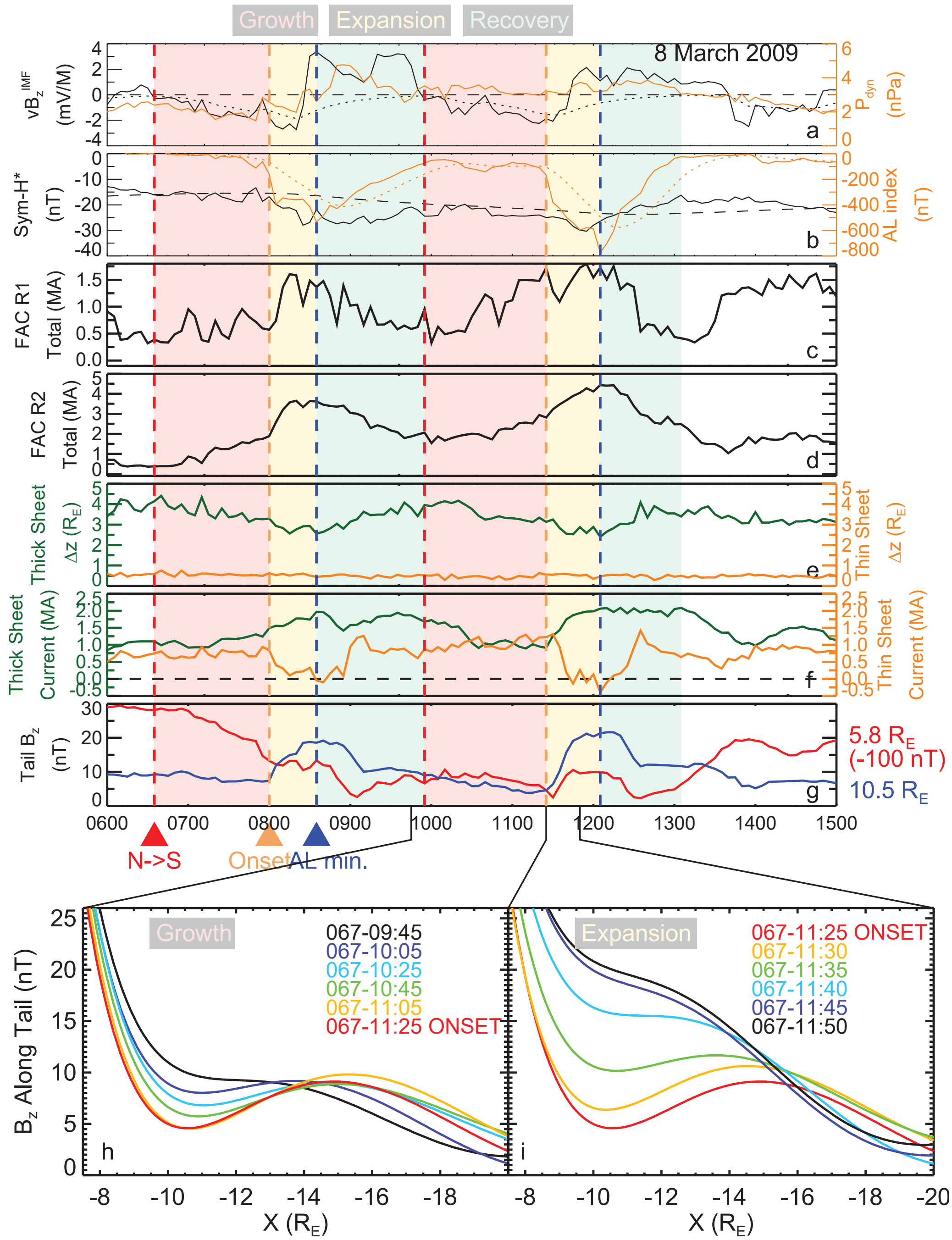

Figure 6. Analysis of the March 8, 2009 substorm current system evolution. (a and b) Solar wind measurements and Geomagnetic indices respectively; similar to panels (e) and (f) in Figure 1 respectively. (c and d) The square root of the sum of the squared amplitude coefficients for the R1 and R2 FAC modules respectively (Sitnov, Stephens, et al., 2017). (e) The equatorial CS half thickness parameter for the thick CS in green and the TCS in orange. (f) The westward current from the thick CS module passing through the dayside rectangle: $1.0\ R_E \leq X \leq 6.616\ R_E$ and $-5.0\ R_E \leq Z \leq 5.0\ R_E$ in green and the westward current from the TCS module passing through the magnetotail rectangle: $-16\ R_E \leq X \leq -6\ R_E$ and $-1.0\ R_E \leq Z \leq 1.0\ R_E$ in orange. (g) Total modeled B_z sampled at $\boldsymbol{r} = (-5.8\ R_E, 0, 0)$ in red and $\boldsymbol{r} = (-10.5\ R_E, 0, 0)$ in blue. (h and i) The total modeled B_z sampled along the line $(-20\ R_E \leq X \leq -7.5\ R_E, 0, 0)$ during the growth phase and expansion phase respectively.

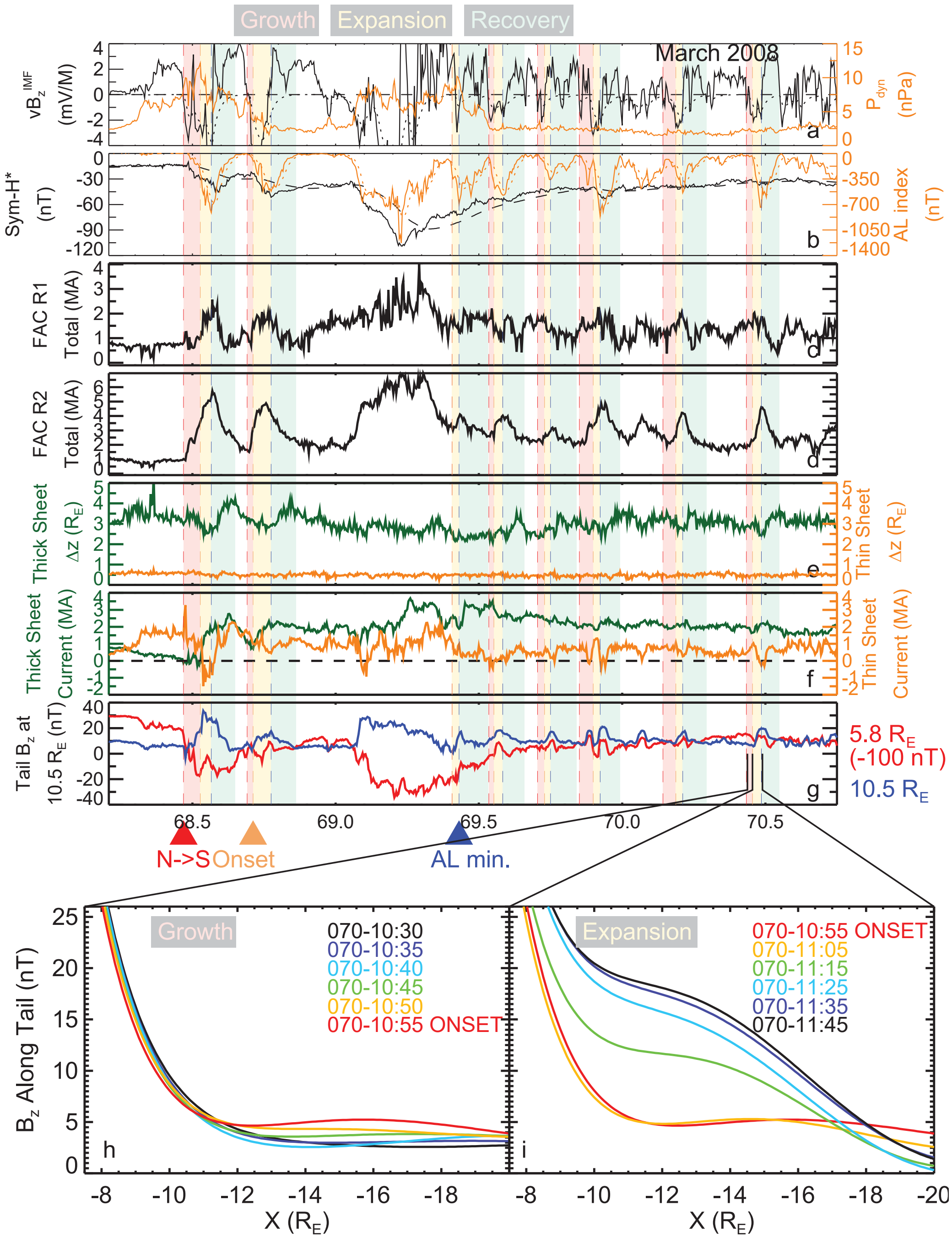

Figure 7 Analysis of the March 2008 storm containing substorms, substorm current system evolution. The panels are the same as in Figure 6 but except for a different event.

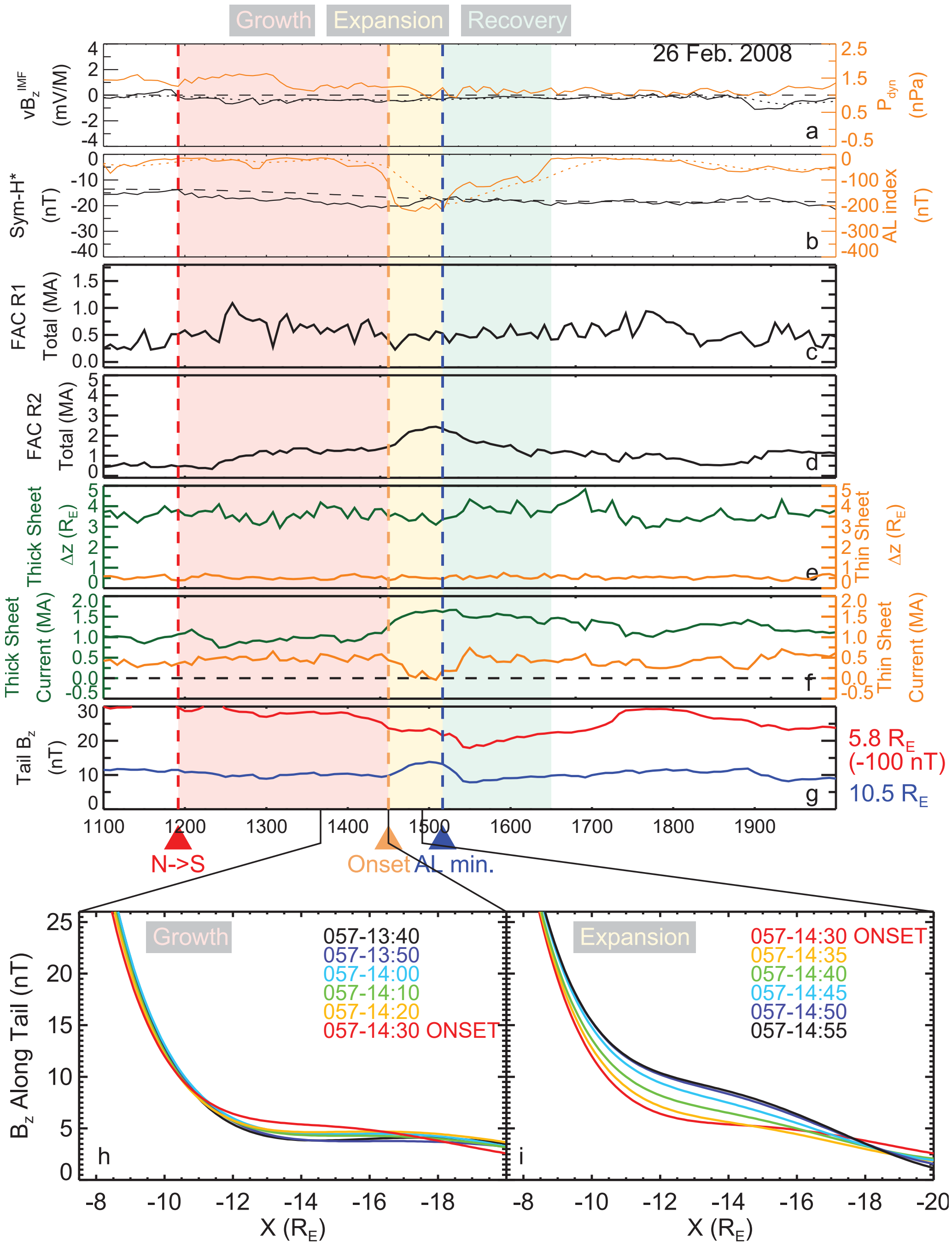

636 **Figure 8** Analysis of the February 26, 2008 substorm current system evolution. The panels are the same as in
637 Figure 6 but except for a different event.

The analysis of a relatively weak non-storm substorm, which occurred 26 February 2008, is presented in Figure 8 (the corresponding validation results are provided in Figure S4). It confirms the general nature of some key substorm features that have been conjectured before but are now seen with statistical significance for a range of different types of substorms. These include the rapid disappearance of the TCS in the expansion phase (Figure 8f, orange line) accompanied by the more gradual and long-lasting increase and accumulation of the thick CS (Figure 8f, green line), B_z dipolarization at 10.5 R_E correlated with a signal at 5.8 R_E, which however may not have the similar form (compare Figure 8g and the first event in Figure 6g with the second event in the same figure as well as in Figure 7g). The generic nature of thinning and dipolarization processes, including the evolution of TCS and thick CS components, is confirmed by supplementary Figures S5–S10, which show analogs of Figures 3–5 for 10 March and 26 February 2008 substorms.

At the same time, Figure 8h, in contrast to Figures 6h and 7h, does not show the formation of a B_z hump in the late growth phase. One can suggest that it is either forming earlier (black line) or further away from the Earth, where the empirical reconstruction is less robust because of the lack of data. Also, vB_z^{IMF} is relatively weak prior to the substorm, so it is possible that the growth phase of this particular substorm is not fully captured by the parameter derived from vB_z^{IMF} described in equation (8). The specific conditions favorable for the hump formation and determining its location in the tail are still to be investigated.

A common feature for all events considered here is the increase of the FAC R2 magnitude, first in the growth phase and then a more rapid enhancement in the expansion phase. It is not accompanied by the corresponding enhancement of the higher-latitude R1 current part for the weak storm shown in Figure 8c. For stronger storms shown in Figures 6c and 7c the concurrent R1 is present, but its shape is not so similar to the substorm variation expressed in terms of the *AL* index. One should stress here that the amplitudes R1 and R2 shows in panels Figures 6c–8c only reflect the strength of the corresponding high- and low-latitude currents, but not their R1/R2sense. The detailed structure of these currents, including their 3-D features will described in the next section.

3.4 3-D picture of substorm currents and the substorm current wedge

Figure 9 provides 3-D distributions of magnetospheric currents in different phases of the March 2009 substorm, corresponding to Figures 3, 4, and 5, whereas Figure 10 provides the reconstruction of the current systems associated with the substorm expansion.

Figures 9a–9c confirm the TCS buildup, decay and rebuilding shown by an orange volume rendering and reflected by 2-D slices in Figures 3–5. The evolution of the thick CS shown by the meridional cut of the corresponding contribution to the total current density is different from the TCS evolution, and of particular interest is the persistence of the thick CS in the recovery phase. Mapping of selected 3-D current loops in Figure 9b (see also Figure 5d) shows that the thick CS is closed through the ionosphere via R2-type FAC system similar to the storm-time PRC.

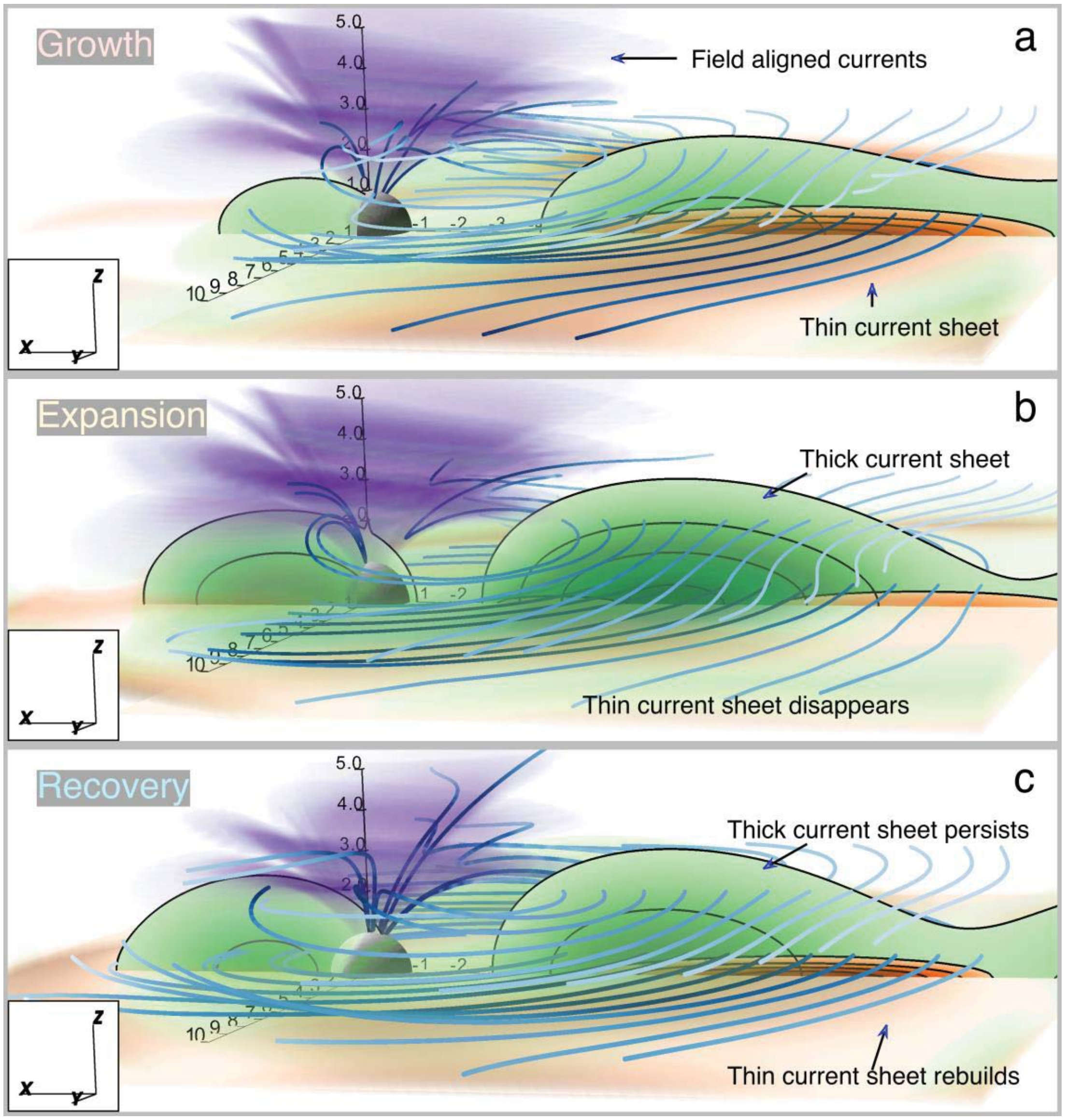

Figure 9. 3-D reconstruction of major current systems for the March 8, 2009 substorm. (a) growth phase; (b) expansion phase; (c) recovery phase. An orange volume rendering shows the 3-D distribution of the TCS and a violet volume rendering shows the FAC distribution. The 3-D distribution of the thick CS is shown by a 3-D green volume rendering and it is complemented by the 2-D distribution of the current along the midnight meridian. Blue contours show selected current lines and their intensity reflects the current strength.

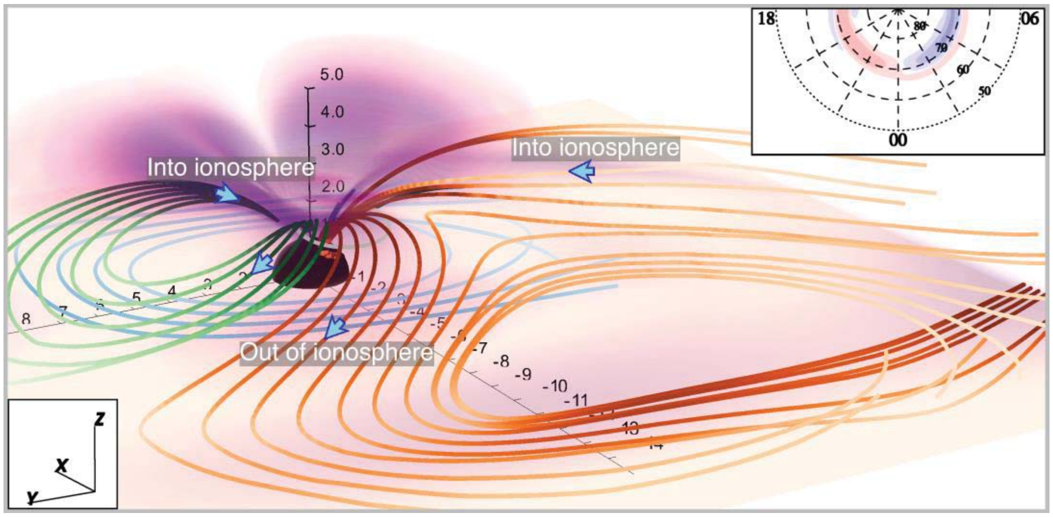

Figure 10. 3-D reconstruction of SCW for the March 8, 2009 substorm. Currents present are obtained by taking the curl of the difference between the magnetic fields in the expansion and growth phase currents. A violet volume rendering shows the 3-D distribution of the currents, while selected current lines feature the classical SCW (dark orange lines), R2 currents similar to the PRC storm-time current (green lines), and symmetric ring current (blue lines). The inset in the format of Figure 3c displays the FAC distribution of 3-D currents, and in particular, the low-altitude portion of the SCW.

The distinctive features of the substorm current system reconfigurations are presented in Figure 10, which shows 3-D currents obtained from the difference between the magnetic field in the expansion phase (Figure 4) and the growth phase (Figure 3). Currents in Figure 10 are computed by applying Ampere's law to the difference between the expansion (11:50) and growth phase (11:25). In order to simplify this picture, the growth phase used in this difference calculation was fit in a different manner. The non-linear parameters were not fit but were instead set to be identical to the expansion phase. For example, this forces the FAC distributions from the growth and expansion phases to coalign, making for a simpler picture when the difference is computed. Additionally, for simplicity the dipole tilt deformations are turned off by setting the parameters that control this deformation (hinging, warping, and twisting parameters) to zero. This aligns the magnetic equator in the equatorial plane.

The inset in Figure 10 shows that the low-altitude FAC system has the spiral pattern similar to that of the total field in each phase. However, this spiral is shifted to low latitudes, compared to the growth phase pattern (Figure 3c). Figure 10, together with Figure 11, show that the spiral pattern is a set of foot points of the R1-sense SCW loop (orange lines), which had been conjectured (Crooker & McPherron, 1972; Fukushima & Kamide, 1973; McPherron et al., 1973) based on a limited number of ground-based and spaceborne observations. Figure 10 also confirms the appearance of closed near-equatorial SCW loops predicted based on MHD simulations of magnetotail dipolarizations (loop #3 in Plate 4 in (Birn et al., 1999) further generalized to a combination of loops #3 and 4 in Fig. 5 in (Kepko et al., 2015)). Although the earthward propagation of the dipolarization signal deep into the geosynchronous region is clearly seen from data (compare black and red lines in Figure 6g), Figure 10 does not show a separate R2 current system earthward of the SCW, which was predicted as a precursor of dipolarizing flux tubes based on MHD and kinetic simulations (Birn et al., 1999; Yang et al., 2011). This may be caused by either yet insufficient spatial resolution of our empirical picture or by transient nature of R2 FAC precursors on the time scales smaller than those of substorms. At the same time, Figure 10 reveals two large-scale current systems apparently associated with the buildup of the storm-time currents: the R2 loop located right clockwise of the SCW (green lines) resembling the PRC, and another current loop encircling the Earth and similar to the symmetric ring current (SRC).

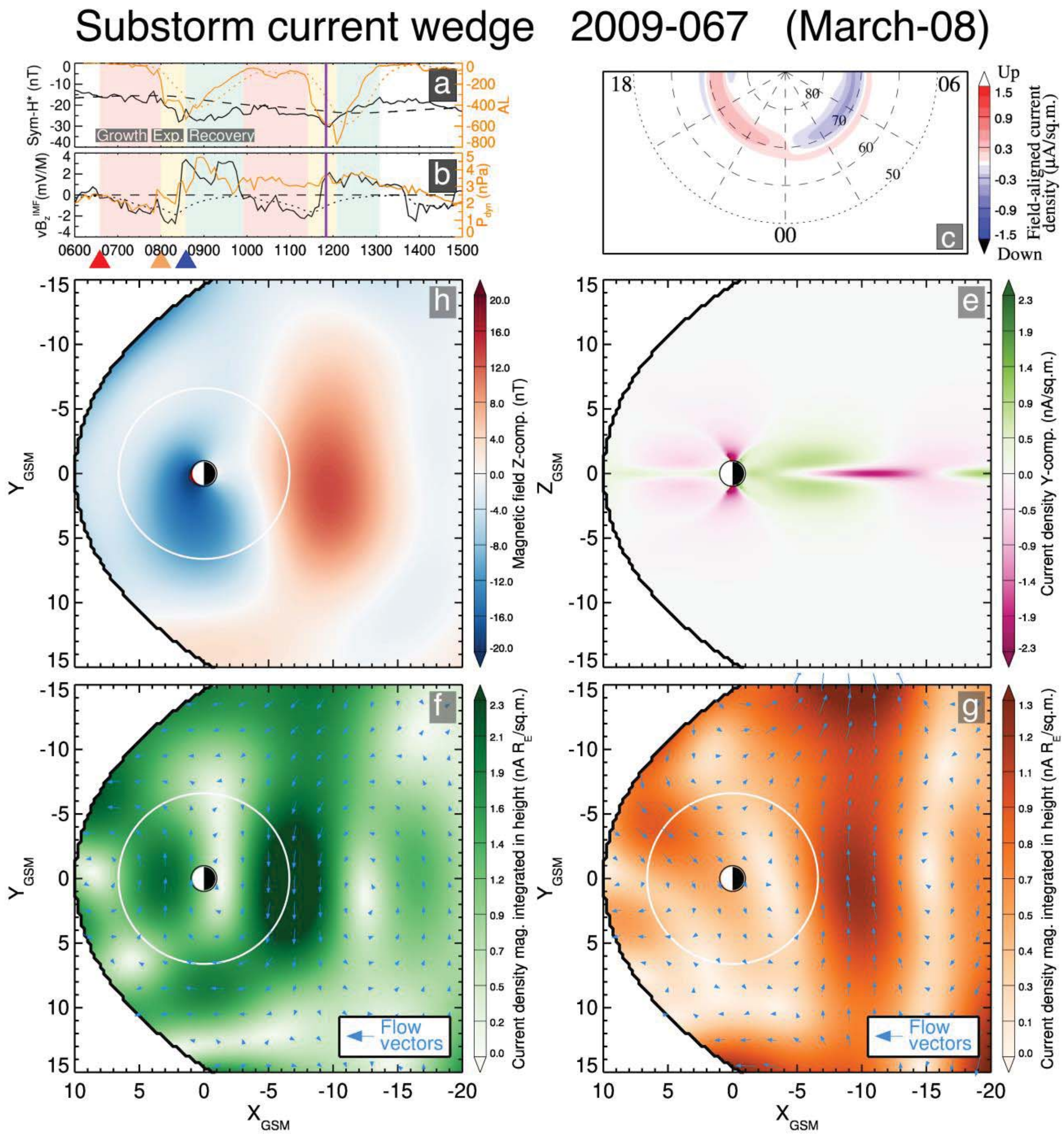

Figure 11. 2-D reconstruction of the substorm expansion currents of the March 8, 2009 substorm (2-D analog of Figure 6). The panels are similar to Figures 3–5 but except now are the difference between the expansion phase and the growth phase. The ionospheric closure of the SCW in panel (c) is shown centered about midnight and flows in the same sense as a R1 FAC. The equatorial slice of the differenced magnetic field in panel (d), reflects the magnetic flux buildup region centered in the premidnight sector and at $X \sim -10\ R_E$. Also seen, is a decrease in the magnetic field from pre-noon through the post-dusk sector within Geosynchronous orbit caused by the buildup of a westward

ring current. Panel (e) shows the meridional slice of the *Y*-component of the differenced current density. The equatorial portion of the SCW can be seen in this panel as the eastward TCS centered at $X \sim -10\ R_E$. It partially closes through the westward thick CS shown in the same panel and also partially closes through the ionosphere as is shown in Figure 10. On the dayside within Geosynchronous orbit, the thick CS is westward, indicating a ring current. Panels (f) and (g) show the equatorial slice of the height integrated magnitude of the differenced current density for the thick and thin CSs. The equatorial portion of the SCW shown in panel (g) is flowing eastward and is centered in the premidnight sector at $X \sim -10\ R_E$. Meanwhile a westward thick CS shown in panel (f), is enhanced in the region centered about midnight at $X \sim -7\ R_E$. Part of this enhancement is seen to be the closure of the SCW in Figure 10, while part of it flows out to the pre-dusk magnetopause. Yet additional current flows around to the dayside, forming a symmetric ring current part. There is an additional smaller dusk enhancement at $Y \sim 8\ R_E$. As was shown in Figure 10, this partially closes through the ionosphere, forming a PRC.

The qualitative picture of substorms and storms, including the SCW, PRC and SRC systems, was conjectured almost half a century ago based largely on ground-based observations of the magnetic field by Crooker and McPherron (1972) as well as Kamide & Fukushima (1972) (see in particular, Figs. 22 and 23 in (Fukushima & Kamide, 1973)). However, only now the quantitative reconstruction of the 3-D structure of all these currents and their evolution directly from spaceborne magnetometer data has become possible. The generic nature of the obtained substorm features shown here for the March 2009 event is confirmed by similar results obtained for the March 2008 storm-time substorms (Figures 1, 7 and S5–S7) and a much weaker substorm that occurred on 26 February 2008 (Figures 8 and S8–S10). Also noteworthy, is that the magnetic field dipolarization in the expansion phase clearly shows that the magnetic flux is redistributed earthward (seen from the comparison between Figures 3d and 3e, on the one hand, and 4d and 4e, on the other, as well from the comparison of panels (h) and (i) in Figures 6–8), which is consistent with in situ observations by multi-probe missions (Ohtani, 1998; Angelopoulos et al., 2008) and confirms the statistical significance of the corresponding fortuitous substorm case studies. For example, as is seen from Figure 6g, during the second event of the March 2009 substorms, the beginning of the dipolarization is observed at 10.5 R_E in the tail tens of minutes before it is seen to begin at 5.8 R_E (approximately the apogee of the Van Allen spacecraft). In the first weaker substorm, the dipolarization never reaches 5.8 R_E and the field there actually continues to thin. The analysis of March and February 2008 substorms (Figures 7 and 8) confirm that finding.

4 Discussion and Conclusions

We conclude that by data mining more than two decades of multi-mission magnetometer data the global picture of major 3-D current systems that constitute the phenomenon of magnetospheric substorms, as defined by the auroral index *AL*, can be reconstructed. Their evolution is not limited to the stretching and dipolarization of the night-side magnetic field, but also includes the formation and persistence of currents pertinent to magnetic storms. The data-mining approach employed in our study is based on the NN method, which generalizes earlier multi-probe event-oriented reconstructions as well as custom-made statistical models, revealing both the generic thinning/dipolarization signatures and also the individual features of the event of interest. It should be stressed that in this paper we do not introduce another “fully cooked” geomagnetic field model, like T89, TS05 and other classical Tsyganenko models (e.g., Tsyganenko, 2013, and refs. therein). We rather introduce a method of the empirical analysis of the magnetospheric configuration during substorms, and we provide the first proof-of-principle demonstration that this method works.

This approach assumes the state of the magnetosphere during substorms can be determined by the 5-D state vector defined by equations (4)–(8) and locates magnetometer data from the historical database from events closest to the moment of interest using a Euclidean distance metric represented by equation (9). Thus, the data-mining approach lies in between event based studies that use simultaneous in situ measurements to infer substorm dynamics and large statistical studies that average over all the available substorms. As this study shows, the approach is capable of distinguishing substorm phases, identifying the mixed nature of storm-time substorms, and distinguishes between strong (8 March 2009) and weaker (26 February 2008) substorms. This technique is still limited in reproducing some details of individual events, as is seen from our validation tests (Figures 1, 2, and S4). In particular, the magnitude of both the current sheet thinning signatures in B_x and the dipolarization signatures in B_z are often underestimated in the reconstructions as compared to the in situ magnetometer data. This may be the result of averaging over numerous substorms and thus spreads these signatures over a larger local time. Additionally, the *AL* index contains little information about the local time location and extent of the dipolarization and associated substorm current wedge. This may explain the discrepancy between the reconstructed B_z component of the magnetic field and the GOES-11 magnetometer data during the expansion phase of the 8 March 2009 event (Figure 2t). GOES-11 is located at ~3 MLT, however, Figure 4d and 4f indicate the reconstructed dipolarization does not penetrate that far dawnward. Another contributing factor may be a result of the dimensionality of the NN parameter space. By minimizing the distance in a 5-D parameter space, the sensitivity of any single parameter is decreased. For example, the second substorm on 8 March 2009 has a minimum value of smoothed *AL* of -576 nT, while the average of the NNs selected for this reconstruction is only -423 nT. This can be mitigated by increasing the corresponding weight factor of any given parameter in the distance metric in equation (9), but as of now this investigation has not been done. There is also perhaps a shortcoming in the use of the smoothed vB_s^{IMF} parameter to identify the growth phase. Of the three growth phase tail B_z profiles plotted in Figures 6–8h, only Figure 6h had a strongly defined tailward B_z gradient, which of the three, had strongest smoothed vB_s^{IMF} profile (Figure 6a dotted black dotted line). In comparison, the growth phase represented in Figure 6h only lasted for 25 minutes as determined by vB_s^{IMF} and the 26 February, while long, was much weaker (vB_s^{IMF} < 0.4 mV/M). Neither of these later types of growth phases will be well captured by equation (8).

This study is limited to relatively conventional isolated substorms with characteristic loading-unloading cycle durations of about 2 hours, consistent with the selected NN parameters (4)–(6). However, the magnetospheric activity reflected by the auroral indices, such as the *AL* index, is not limited to substorms. It also includes longer time-scale phenomena, such as steady magnetospheric convection events (SMC) that represent a mode where this conversion process is quasi-steady and the dayside reconnection rate is assumed to be in balance with the nightside rate. Like substorms, this class of events is frequently defined from auroral indices, often a stable and continuous level of *AL* activity, and they are sustained by stably southward IMF (Sergeev, Pellinen et al. 1996). As such, there is overlap between substorms and SMC based purely on *AL* and solar wind parameters such as vB_s^{IMF}. This demonstrates the importance of including the time derivatives of the parameters in the NN approach. SMC events were previously analyzed with the TS07D model (Stephens et al., 2013), and in particular it was found these events possessed a tailward B_z gradient. However, the $B_z(x)$ profiles were found to differ substantially. The early part of the SMC event possessed a deep B_z minimum (similar to the onset profile in Figure 6h), but as the SMC event progressed the B_z minimum became shallower and moved earthward. The advancements presented here may be useful in discerning the variety of magnetotail configurations that exist in these different convection modes and how they relate to one another. However, due to the long duration and relatively rarity of SMCs compared with substorms (O'Brien et al., 2002), the DM technique may be customized for SMCs by adding longer duration *AL* parameters similar to those in equations (6) and (7) but with a smoothing timescale on the order of SMC intervals.

At the same time, the present analysis averaged over many interesting substorm phenomena on the scales smaller than those of the global magnetospheric reconfiguration during a substorm. They include bursty bulk flows, dipolarization fronts, ballooning/interchange, and flapping motions of the plasma sheet, as well as wedgelets (e.g., Sergeev et al., 2006; Runov et al., 2012; Liu et al., 2013; Kepko et al., 2015, and refs. therein) and their ionospheric manifestations (Keiling et al., 2013; Henderson, 2013). These phenomena are very important to understand substorm mechanisms (e.g., Sergeev, Pulkkinen et al., 1996), but they are hard to reconstruct using any global empirical reconstruction of the magnetic field. They can be investigated, however, using local observations (Sergeev, Angelopoulos et al., 2011), global MHD (Wiltberger et al., 2000; Raeder et al., 2008), and local kinetic (Yang et al., 2011; Sitnov, Merkin et al., 2017) simulations of the magnetosphere. It is interesting that the latter reveal the importance of the global structure of the magnetosphere (for instance, through the flux tube volume parameter) for substorm plasma instabilities (Sitnov, Merkin et al., 2017; Birn et al., 2018).

Thus, the obtained empirical picture of substorms may be decisive for understanding their underlying physical mechanisms and for interpreting similar substorm-like phenomena on other planets (Mitchell et al., 2009; Slavin et al., 2010), in the solar corona (Reeves et al., 2008), and on other astrophysical objects (Osten et al., 2016) where such a comprehensive coverage in space and time is impossible.

Acknowledgments, Samples, and Data

This work was funded by NASA grants NNX15AF53G, NNX16AB78G, NNX16AB80G, as well as NSF grants AGS-1702147 and AGS-1744269. We thank the many spacecraft and instrument teams and their PIs who produced the datasets we used in this study, including the Cluster, Geotail, Polar, Imp-8, GOES, THEMIS, and Van Allen Probes, particularly their magnetometer teams. We also thank, the SPDF for the OMNI database for solar wind values, which is composed of datasets from the IMP-8, ACE, WIND, Geotail, and DSCOVR missions, and also the WDC in Kyoto, for the Geomagnetic indices. We gratefully acknowledge the SuperMAG collaborators (http://supermag.jhuapl.edu/info/?page=acknowledgement) for use of their substorm onset list. We also want to thank Don Mitchell, Ed Roelof, and Ralph McNutt for useful discussions. The compiled magnetometer database used in this study is available on the SPDF website (https://spdf.gsfc.nasa.gov/pub/data/aaa_special-purpose-datasets/empirical-magnetic-field-modeling-database-with-TS07D-coefficients/). The model output is available on request and will be archived.

References

Akasofu, S. I. (1964). The development of the auroral substorm. *Planetary and Space Science,* 12, (4), 273–282. doi:10.1016/0032-0633(64)90151-5

Angelopoulos, V., McFadden, J. P., Larson, D., Carlson, C. W., Mende, S. B., Frey, H., Phan, T., Sibeck, D. G., Glassmeier, K.-H., Auster, U., Donovan, E., Mann, I. R., Rae, I. J., Russell, C. T., Runov, A., Zhou, X.-Z., & Kepko, L. (2008). Tail reconnection triggering substorm onset. *Science,* 321, (5891), 931-935. doi:10.1126/science.1160495

Angelopoulos, V., Runov, A., Zhou, X.-Z., Turner, D. L., Kiehas, S. A., Li, S.-S., & Shinohara, I. (2013). Electromagnetic energy conversion at reconnection fronts. *Science,* 341, (6153), 1478–1482. doi:10.1126/science.1236992

Artemyev, A. V., Angelopoulos, V., Runov, A., & Petrokovich, A. A. (2016). Properties of current sheet thinning at $x \sim -10$ to -12 R_E, *Journal of Geophysical Research: Space Physics*, 121, 6718–6731, doi: 10.1002/2016JA022779

Baker, D. N., et al. (2016). A telescopic and microscopic examination of acceleration in the June 2015 geomagnetic storm: Magnetospheric Multiscale and Van Allen Probes study of substorm particle injection, *Geophysical Research Letters*, 43, 6051–6059, doi: 10.1002/2016GL069643

Birn, J., Hesse, M., Haerendel, G., Baumjohann, W., & Shiokawa, K. (1999). Flow braking and the substorm current wedge. *Journal of Geophysical Research,* 104, (A9) 19895–19903. doi:10.1029/1999JA900173

Birn, J., Merkin, V. G., Sitnov, M. I., & Otto, A. (2018). MHD stability of magnetotail configurations with a B_z hump. *Journal of Geophysical Research: Space Physics*, 123, 3477–3492. https://doi.org/10.1029/2018JA025290

Blanchard, G. T., & McPherron, R. L. (1995). Analysis of the linear response function relating AL to VBs for individual substorms. *Journal of Geophysical Research,* 100, (A10), 19,155–19,165, doi:10.1029/95JA01341

Boteler, D. H. (2001). Space Weather Effects on Power Systems. In *Space Weather, Geophysical Monograph Series*, P. Song, H. J. Singer, G. L. Siscoe. AGU, Washington D.C., pp. 347–352, doi:10.1029/GM125p0347

Burch, J. L., Torbert, R. B., Phan, T. D., Chen, L.-J., Moore, T. E., Ergun, R. E., et al. (2016). Electron-scale measurements of magnetic reconnection in space. *Science*, 352(6290), aaf2939. https://doi.org/10.1126/science.aaf2939

Burton, R. K., McPherron, R. L., & Russell, C. T. (1975). An Empirical Relationship Between Interplanetary Conditions and Dst. *Journal of Geophysical Research,* 80, (31), 4204–4214, (1975). doi:10.1029/JA080i031p04204

Chapman, S. (1962). Earth storms: Retrospect and prospect, *Journal of the Physical Society of Japan,* 17, (Suppl. A-I), 6–16.

Connors, M., Russell, C. T., & Angelopoulos, V. (2011). Magnetic flux transfer in the 5 April 2010 Galaxy 15 substorm: An unprecedented observation. *Annales Geophysicae,* 29, 619–622. doi:10.5194/angeo-29-619-2011

Crooker, N. U., & McPherron, R. L. (1972). On the distinction between the auroral electrojet and partial ring current systems, *Journal of Geophysical Research,* 77, (34), 6886–6889. doi:10.1029/JA077i034p06886

Davis, T. N., & Sugiura, M. (1966). Auroral electrojet activity index AE and its universal time variations. *Journal of Geophysical Research,* 71, (3), 785–801. doi:10.1029/JZ071i003p00785

Erkaev, N.V., Semenov, V.S., & Biernat, H.K. (2007). Magnetic double-gradient instability and flapping waves in a current sheet. *Physical Review Letters*, 99, 235003. doi:10.1103/PhysRevLett.99.235003, 2007.

Fukushima, N., & Kamide, Y. (1973). Partial ring current models for worldwide geomagnetic disturbances. *Reviews of Geophys*ics, 11, (4), 795–853. doi:10.1029/RG011i004p00795

Gjerloev, J. W. (2012), The SuperMAG data processing technique, *Journal of Geophysical Research: Space Physics*, 117, A09213. doi:10.1029/2012JA017683

Harang, L. (1946). The Mean Field of Disturbance of Polar Geomagnetic Storms. *Terr. Magn. Atmos. Electr.,* 51, (3), 353–380. doi:10.1029/TE051i003p00353

Henderson, M. G. (2013). Auroral Substorms, Poleward Boundary Activations, Auroral Streamers, Omega Bands, and Onset Precursor Activity. In Auroral Phenomenology and Magnetospheric Processes: Earth And Other Planets (eds A. Keiling, E. Donovan, F. Bagenal and T. Karlsson). doi:10.1029/2011GM001165

Iijima, T., & Potemra, T. A. (1976). Field-aligned currents in the dayside cusp observed by Triad. *Journal of Geophysical Research,* 81, (34), 5971–5979. doi:10.1029/JA081i034p05971

Iyemori, T. (1990). Storm-time magnetospheric currents inferred from mid-latitude geomagnetic field variations. *Journal of Geomagnetism and Geoelectr*icity, 42, (11), 1249–1265 (1990). doi:10.5636/jgg.42.1249

Kamide, Y., (1992). Is substorm occurrences a necessary condition for a magnetic storm?, *J. Geomag. Geoelectr.*, 44, 109–117. doi:10.5636/jgg.44.109

Kamide, Y., Baumjohann, W., Daglis, I., Gonzalez, W., Grande, M., Joselyn, J., et al. (1998). Current understanding of magnetic storms: Storm-substorm relationships. *Journal of Geophysical Research*, 103 (A8), 17,705–17,728. doi:10.1029/98JA01426

Kamide, Y. & Fukushima, N. (1972). Positive Geomagnetic Bays in Evening High Latitudes and Their Possible Connection with Partial Ring Current. *Rep. Ionosphere Space Res. Jap.* 26, 79–101

Keiling, A. , Shiokawa, K. , Uritsky, V. , Sergeev, V. , Zesta, E. , Kepko, L. and Østgaard, N. (2013). Auroral Signatures of the Dynamic Plasma Sheet. In Auroral Phenomenology and Magnetospheric Processes: Earth And Other Planets (eds A. Keiling, E. Donovan, F. Bagenal and T. Karlsson). doi:10.1029/2012GM001231

Kepko, L., McPherron, R. L., Amm, O., Apatenkov, S., Baumjohann, W., Birn, J., Lester, M., Nakamura, R., Pulkkinen, T. I., & V. Sergeev (2015), Substorm current wedge revisited, *Space Science Reviews*, 190(1), 1–46. doi:10.1007/s11214-014-0124-9

Kubyshkina, M. V., Sergeev, V. A., & Pulkkinen, T. I. (1999). Hybrid Input Algorithm: An event-oriented magnetospheric model. *Journal of Geophysical Research,* 104, (A11), 24977–24993. doi:10.1029/1999JA900222

Laundal, K. M., & Richmond, A. D. (2017). Magnetic coordinate systems. *Space Science Reviews,* 206, (1-4), 27–59. doi:10.1007/s11214-016-0275-y

Liu, J., V. Angelopoulos, A. Runov, and X.-Z. Zhou (2013), On the current sheets surrounding dipolarizing flux bundles in the magnetotail: The case for wedgelets, *J. Geophys. Res. Space Physics*, 118, 2000–2020, doi: 10.1002/jgra.50092

Machida, S., Miyashita, Y., Ieda, A., Nose, M., Nagata, D., Liou, K., T. Obara, T., Nishida, A., Saito, Y., & Mukai T. (2009). Statistical visualization of the Earth's magnetotail based on Geotail data and the implied substorm model, *Annales Geophysicae*, 27, 1035. doi: 10.5194/angeo-27-1035-2009

McComas, D. J., et al. (2011), First IBEX observations of the terrestrial plasma sheet and a possible disconnection event, *Journal of Geophysical Research*, 116, A02211, doi: 10.1029/2010JA016138

McPherron, R. L. (2016), Where and when does reconnection occur in the tail?, *J. Geophys. Res. Space Physics*, 121, 4607–4610, doi: 10.1002/2015JA022258

McPherron, R. L., Russell, C. T., & Aubry, M. P. (1973). Satellite studies of magnetospheric substorms on August 15, 1968: 9. Phenomenological model for substorms. *Journal of Geophysical Research,* 78, (16), 3131–3149. doi:10.1029/JA078i016p03131

McPherron, R. L., & Chu, X. (2017). The mid-latitude positive bay and the MPB Index of substorm activity. *Space Science Reviews,* 206, (1-4), 91–122. doi:10.1007/s11214-016-0316-6

Merkin, V. G., Sitnov, M. I., & Lyon J. G. (2015), Evolution of generalized two-dimensional magnetotail equilibria in ideal and resistive MHD. *Journal of Geophysical Research: Space Physics*, 120, 1993–2014. doi: 10.1002/2014JA020651

Merkin, V. G., & Sitnov M. I. (2016), Stability of magnetotail equilibria with a tailward B_z gradient. *Journal of Geophysical Research: Space Physics*, 121, 9411–9426, doi: 10.1002/2016JA023005

Mitchell, T.M. (1997). *Machine Learning*, first ed. McGraw-Hill, Inc., New York, NY

Mitchell, D. G., J. F. Carbary, S. W. H. Cowley, T. W. Hill, and P. Zarka (2009). The dynamics of Saturn's magnetosphere, in *Saturn From Cassini-Huygens*, edited by M. K. Dougherty, L. W. Esposito, and S. M. Krimigis, p. 257, Springer, Dordrecht, and New York

Murphy, K. R., Mann, I. R., Rae, I. J., Waters, C. L., Frey, H. U., Kale, A., Singer, H. J., Anderson, B. J., & Korth, H. (2013). The detailed spatial structure of field-aligned currents comprising the substorm current wedge. *Journal of Geophysical Research,* 118, (12), 7,714–7,727. doi: 10.1002/2013JA018979

Newell, P. T., & Gjerloev, J. W. (2011), Evaluation of SuperMAG auroral electrojet indices as indicators of substorms and auroral power. *Journal of Geophysical Research: Space Physics*, 116, A12211. doi:10.1029/2011JA016779

Newell, P. T., & Gjerloev, J. W. (2011), Substorm and magnetosphere characteristic scales inferred from the SuperMAG auroral electrojet indices. *Journal of Geophysical Research: Space Physics*, 116, A12232. doi:10.1029/2011JA016936

Newell, P. T., Sotirelis, T., Liou, K., Meng, C.-I., & Rich, F. J. (2007). A nearly universal solar wind-magnetosphere coupling function inferred from 10 magnetospheric state variables. *Journal of Geophysical Research,* 112, A01206. doi:10.1029/2006JA012015

O'Brien, T. P., Thompson, S. M., & McPherron R. L. (2002). Steady magnetospheric convention: Statistical signatures in the solar wind and *AE*. *Geophys. Res. Lett.*, 29 (7). doi: 10.1029/2001GL014641

Ohtani, S. (1998), Earthward expansion of tail current disruption: Dual-satellite study, *Journal of Geophysical Research*, 103(A4), 6815–6825, doi: 10.1029/98JA00013

Ohtani, S., & Motoba, T. (2017). Equatorial magnetic field of the near-Earth magnetotail, *Journal of Geophysical Research: Space Physics*, doi:10.1002/2017JA024115, 2017.

Osten, R. A., Kowalski, A., Drake, S. A., Krimm, H., Page, K., Gazeas, K., Kennea, J., Oates, S., Page, M., de Miguel, E., Novák, R., Apeltauer, T., & Gehrels, N. (2016). A very bright, very hot, and very long flaring event from the M dwarf binary system DG CVn. *Astrophys. J.*, 832, 174. doi:10.3847/0004-637X/832/2/174

Partamies, N., Juusola, L., Tanskanen, E., & Kauristie, K. (2013). Statistical properties of substorms during different storm and solar cycle phases. *Annales Geophysicae,* 31, 349–358. doi:10.5194/angeo-31-349-2013

Petrukovich, A. A., Artemyev, A. V., Nakamura, R., Panov, E. V., & Baumjohann, W. (2013). Cluster observations of $\partial B_z/\partial x$ during growth phase magnetotail stretching intervals, *Journal of Geophysical Research: Space Physics*, 118, 5720–5730, doi: 10.1002/jgra.50550, 2013.

Press, W. H., Teukolsky, S. A., Vetterling, W. T., & Flannery, B. P. (1992). *Numerical recipes in Fortran 77*, Cambridge, ed. 2, pp. 51–63

Pritchett, P. L., & Coroniti, F. V. (2013). Structure and consequences of the kinetic ballooning/interchange instability in the magnetotail, *Journal of Geophysical Research: Space Physics sics*, 118, 146–159, doi: 10.1029/2012JA018143

Pulkkinen, T. I., Baker, D. N., Fairfield, D. H., Pellinen, R. J., Murphree, J. S., Elphinstone, R. D., McPherron, R. L., Fennell, J. F., Lopez, R. E., & Nagai, T. (1991). Modeling the growth phase of a substorm using the Tsyganenko Model and multi-spacecraft observations: CDAW-9. *Geophysical Research Letters,* 18, (11), 1963–1966. doi:10.1029/91GL02002

Raeder, J., D. Larson, W. Li, L. Kepko, and T. Fuller-Rowell (2008), OpenGGCM simulations for the THEMIS mission, *Space Sci. Rev.,* 141, 535–555

Reeves, G. D., McAdams, K. L., Friedel, R. H. W., & O'Brien, T. P. (2003). *Geophysical Research Letters,* 30, 1529. doi:10.1029/2002GL016513.

Reeves, K. K., Guild, T. B., Hughes, W. J., Korreck, K. E., Lin, J., Raymond, J., Savage, S., Schwadron, N. A., Spence, H. E., Webb, D. F., & Wiltberger, M. (2008). Posteruptive phenomena in coronal mass ejections and substorms: Indicators of a universal process? *Journal of Geophysical Research,* 113, (A9), A00B02. doi:10.1029/2008JA013049

Rostoker, G. (1972). Geomagnetic Indices. *Reviews of Geophys*ics, 10, (4), 935–950. doi:10.1029/RG010i004p00935

Runov, A., Sergeev, V. A., Nakamura, R., Baumjohann, W., Apatenkov, S., Asano, Y., Takada, T., Volwerk, M., Vörös, Z., Zhang, T. L., Sauvaud, J.-A., Rème, H., Balogh, A. (2006). Local structure of the magnetotail current sheet: 2001 Cluster observations. *Annales Geophysicae,* 24, 247–262. doi:10.5194/angeo-24-247-2006

Runov, A., V. Angelopoulos, and X.-Z. Zhou (2012), Multipoint observations of dipolarization front formation by magnetotail reconnection, *J. Geophys. Res*., 117, A05230

Sergeev, V. A., R. J. Pellinen, and T. I. Pulkkinen (1996), Steady Magnetospheric Convection: A Review of Recent Results, *Space Sci. Rev*., 75, 551–604

Sergeev, V. A., T. I. Pulkkinen, and R. J. Pellinen (1996), Coupled-mode scenario for the magnetospheric dynamics, *J. Geophys. Res.*, 101(A6), 13047–13065, doi: 10.1029/95JA03192

Sergeev, V. A., D. A. Sormakov, S. V. Apatenkov, W. Baumjohann, R. Nakamura, A. V. Runov, T. Mukai, and T. Nagai (2006), Survey of large-amplitude flapping motions in the midtail current sheet, *Annales Geophysicae,* 24(7), 2015–2024

Sergeev, V., Angelopoulos, V., Kubyshkina, M., Donovan, E., Zhou, X.-Z., Runov, A., Singer, H., McFadden, J., & Nakamura, R. (2011). Substorm growth and expansion onset as observed with ideal ground-spacecraft THEMIS coverage. *Journal of Geophysical Research,* 116, (A5), A00I26. doi:10.1029/2010JA015689

Sergeev, V. A., Tsyganenko, N. A., Smirnov, M. V., Nikolaev, A. V., Singer, H. J., & Baumjohann, W. (2011). Magnetic effects of the substorm current wedge in a “spread-out wire” model and their comparison with ground, geosynchronous, and tail lobe data. *Journal of Geophysical Research,* 116, (A7), A07218. doi:10.1029/2011JA016471

Sergeev, V. A., Nikolaev, A. V., Tsyganenko, N. A., Angelopoulos, V., Runov, A. V., Singer, H. J., & Yang, J. (2014). Testing a two-loop pattern of the substorm current wedge (SCW2L). *Journal of Geophysical Research,* 119, (2), 947–963. doi:10.1002/2013JA019629

Sergeev, V. A., Gordeev, E. I., Merkin, V. G., & Sitnov, M. I. (2018). Does a local B-minimum appear in the tail current sheet during a substorm growth phase? *Geophysical Research Letters,* 45. doi:10.1002/2018GL077183

Sharma, A. S., Baker, D. N., Grande, M. , Kamide, Y. , Lakhina, G. S., McPherron, R. M., Reeves, G. D., Rostoker, G. , Vondrak, R. and Zelenyiio, L. (2013). The Storm-Substorm Relationship: Current Understanding and Outlook. In Disturbances in Geospace: The Storm-Substorm Relationship (eds A. S. Sharma, Y. Kamide and G. S. Lakhina). doi:10.1029/142GM01

Shue, J.-H., Song, P., Russell, C. T., Steinberg, J. T., Chao, J. K., Zastenker, G., Vaisberg, O. L., Kokubun, S., Singer, H. J., Detman, T. R., & Kawano, H. (1998). Magnetopause location under extreme solar wind conditions. *Journal of Geophysical Research,* 103, (A8), 17,691–17,700. doi:10.1029/98JA01103

Siscoe, G. L., Formisano, V., & Lazarus, A. J. (1968). Relation between geomagnetic sudden impulses and solar wind pressure changes—An experimental investigation. *Journal of Geophysical Research,* 73, (15), 4869–4874 (1968). doi:10.1029/JA073i015p04869

Sitnov, M. I. & Schindler, K. (2010). Tearing stability of a multiscale magnetotail current sheet, *Geophysical Research Lett*ers, 37, L08102, doi:10.1029/2010GL042961

Sitnov, M. I., Tsyganenko, N. A., Ukhorskiy, A. Y., & Brandt, P. C. (2008). Dynamical data-based modeling of the storm-time geomagnetic field with enhanced spatial resolution. *Journal of Geophysical Research,* 113, A07218. doi:10.1029/2007JA013003

Sitnov, M. I., Tsyganenko, N. A., Ukhorskiy, A. Y., Anderson, B. J., Korth, H., Lui, A. T. Y., & Brandt, P. C. (2010). Empirical modeling of a CIR-driven magnetic storm. *Journal of Geophysical Research,* 115, (A7), A07231. doi:10.1029/2009JA015169

Sitnov, M. I., Ukhorskiy, A. Y., & Stephens, G. K. (2012). Forecasting of global data-binning parameters for high-resolution empirical geomagnetic field models. *Space Weather,* 10, (9), S09001. doi:10.1029/2012SW000783

Sitnov, M. I., V. G. Merkin, P. L. Pritchett, and M. Swisdak (2017), Distinctive features of internally driven magnetotail reconnection, *Geophysal Research Letters*, 44, 3028–3037, doi: 10.1002/2017GL072784

Sitnov, M. I., Stephens, G. K., Tsyganenko, N. A., Ukhorskiy, A. Y., Wing, S., Korth, H. and Anderson, B. J. (2017). Spatial Structure and Asymmetries of Magnetospheric Currents Inferred from High-Resolution Empirical Geomagnetic Field Models. In Dawn-Dusk Asymmetries in Planetary Plasma Environments (eds S. Haaland, A. Runov and C. Forsyth). doi:10.1002/9781119216346.ch15

Sitnov, M. I., Stephens, G. K., Gkioulidou, M., Merkin, V. G., Ukhorskiy, A. Y., Korth, H., Brandt P. C., and Tsyganenko, N. A. (2018). Empirical Modeling of Extreme Events: Storm-Time Geomagnetic Field, Electric Current, and Pressure Distributions, In Extreme Events in Geospace, edited by Natalia Buzulukova, Elsevier, pp. 259–279, ISBN 9780128127001, https://doi.org/10.1016/B978-0-12-812700-1.00011-X

Slavin, J. A., Anderson, B. J., Baker, D. N., Benna, M., Boardsen, S. A., Gloeckler, G., Gold, R. E., Ho, G. C., Korth, H., Krimigis, S. M., McNutt, R. L., Nittler, L. R., Raines, J. M., Sarantos, M., Schriver, D., Solomon, S. C., Starr, R. D., Trávnícek, P. M., & Zurbuchen, T. H. (2010). MESSENGER observations of extreme loading and unloading of Mercury's magnetic tail. *Science,* 329, (5992), 665–668. doi:10.1126/science.1188067

Stephens, G. K., Sitnov, M. I., Kissinger, J., Tsyganenko, N. A., McPherron, R. L., Korth, H., & Anderson, B. J. (2013). Empirical reconstruction of storm time steady magnetospheric convection events, *J. Geophys. Res. Space Physics*, 118, 6434–6456, doi: 10.1002/jgra.50592

Stephens, G. K., Sitnov, M. I., Ukhorskiy, A. Y., Roelof, E. C., Tsyganenko, N. A., & Le, G. (2016). Empirical modeling of the storm time innermost magnetosphere using Van Allen Probes and THEMIS data: Eastward and banana currents. *Journal of Geophysical Research,* 121, 157–170. doi:10.1002/2015JA021700

Thébault, E., et al. (2015), International Geomagnetic Reference Field: The 12th generation, *Earth Planets Space*, 67, 79, doi:10.1186/s40623-015-0228-9

Tsyganenko, N. A. (1991). Methods for quantitative modeling of the magnetic field from Birkeland currents. *Planetary and Space Science,* 39, (4), 641-654. doi:10.1016/0032-0633(91)90058-I

Tsyganenko, N. A. (1995). Modeling the Earth's magnetospheric magnetic field confined within a realistic magnetopause. *Journal of Geophysical Research,* 100, (A4), 5,599–5,612. doi:10.1029/94JA03193

Tsyganenko, N. A. (1996), Effects solar wind conditions on the global magnetospheric configuration as deduced from data-based field models. in *Proceedings of the 3rd International Conference of Substorms*, E. J. Rolfe, B. Kaldeich, Eds. (ESA Publ. Div.), pp. 181–185

Tsyganenko, N. A. (1997). An empirical model of the substorm current wedge. *Journal of Geophysical Research,* 102, (A9), 19,935–19,941. doi:10.1029/97JA01904

Tsyganenko, N. A. (1998). Modeling of twisted/warped magnetospheric configurations using the general deformation method. *Journal of Geophysical Research,* 103, (A10), 23,551–23,563 (1998). doi:10.1029/98JA02292

Tsyganenko, N. A. (2002). A model of the magnetosphere with a dawn-dusk asymmetry, 1, Mathematical structure, *Journal of Geophysical Research*, 107(A8), doi: 10.1029/2001JA000219

Tsyganenko, N. A. (2013). Data-based modelling of the Earth's dynamic magnetosphere: A review. *Annales Geophysicae,* 31, 1745–1772. doi:10.5194/angeo-31-1745-2013

Tsyganenko, N. A. & Sitnov, M. I. (2005). Modeling the dynamics of the inner magnetosphere during strong geomagnetic storms. *Journal of Geophysical Research,* 110, (A3), A03208. doi:10.1029/2004JA010798

Tsyganenko, N. A. & Sitnov, M. I. (2007). Magnetospheric configurations from a high-resolution data-based magnetic field model. *Journal of Geophysical Research,* 112, A06225 (2007). doi:10.1029/2007JA012260

Turner, D. L., O'Brien, T. P., Fennell, J. F., Claudepierre, S. G., Blake, J. B., Kilpua, E. K. J., Hietala, H. (2015). The effects of geomagnetic storms on electrons in Earth's radiation belts. *Geophysical Research Letters,* 42, (21), 9176–9184. doi:10.1002/2015GL064747

Wang, C.-P., Lyons, L. R., Nagai, T., and Samson, J. C. (2004). Midnight radial profiles of the quiet and growth-phase plasma sheet: The Geotail observations, Journal of Geophysical Research, 109, A12201. doi:10.1029/2004JA010590

Vassiliadis, D. (2006). Systems theory for geospace plasma dynamics. *Reviews of Geophysics*, 44, (2), RG2002. doi:10.1029/2004RG000161

Weimer, D. R. (1999). Substorm influence on the ionospheric electric potentials and currents. *Journal of Geophysical Research,* 104, (A1), 185–197. doi:10.1029/1998JA900075

Wiltberger, M., T. I. Pulkkinen, J. G. Lyon, and C. C. Goodrich (2000), MHD simulation of the magnetotail during the December 10, 1996, substorm, *J. Geophys. Res.*, 105(A12), 27649–27663, doi: 10.1029/1999JA000251

Wu, X., Kumar, V., Quinlan, J,. Ghosh, J., Yang, Q., Motoda, H., McLachlan, G., Ng, A, Liu, B, Philip, S, et al. (2008). Top 10 algorithms in data mining. Knowl. Inf. Syst., 14, 1–37. doi:10.1007/s10115-007-0114-2

Yang, J., Toffoletto, F. R., Wolf, R. A., & Sazykin, S. (2011). RCM-E simulation of ion acceleration during an idealized plasma sheet bubble injection. *Journal of Geophysical Research,* 116, (A5), A05207. doi:10.1029/2010JA016346

Yue, C., C. -P. Wang, Y. Nishimura, K. R. Murphy, X. Xing, L. Lyons, M. Henderson, V. Angelopoulos, A. T. Y. Lui, and T. Nagai (2015), Empirical modeling of 3-D force-balanced plasma and magnetic field structures during substorm growth phase, *Journal of Geophysical Research: Space Physics*, 120, 6496–6513, doi: 10.1002/2015JA021226

Zou, S., Lyons, L. R., Wang, C.-P., Boudouridis, A., Ruohoniemi, J. M., Anderson, P. C., Dyson, P. L., & Devlin, J. C. (2009). On the coupling between the Harang reversal evolution and substorm dynamics: A synthesis of SuperDARN, DMSP, and IMAGE observations. *Journal of Geophysical Research,* 114, (A1), A01205. doi:10.1029/2008JA013449

F01.

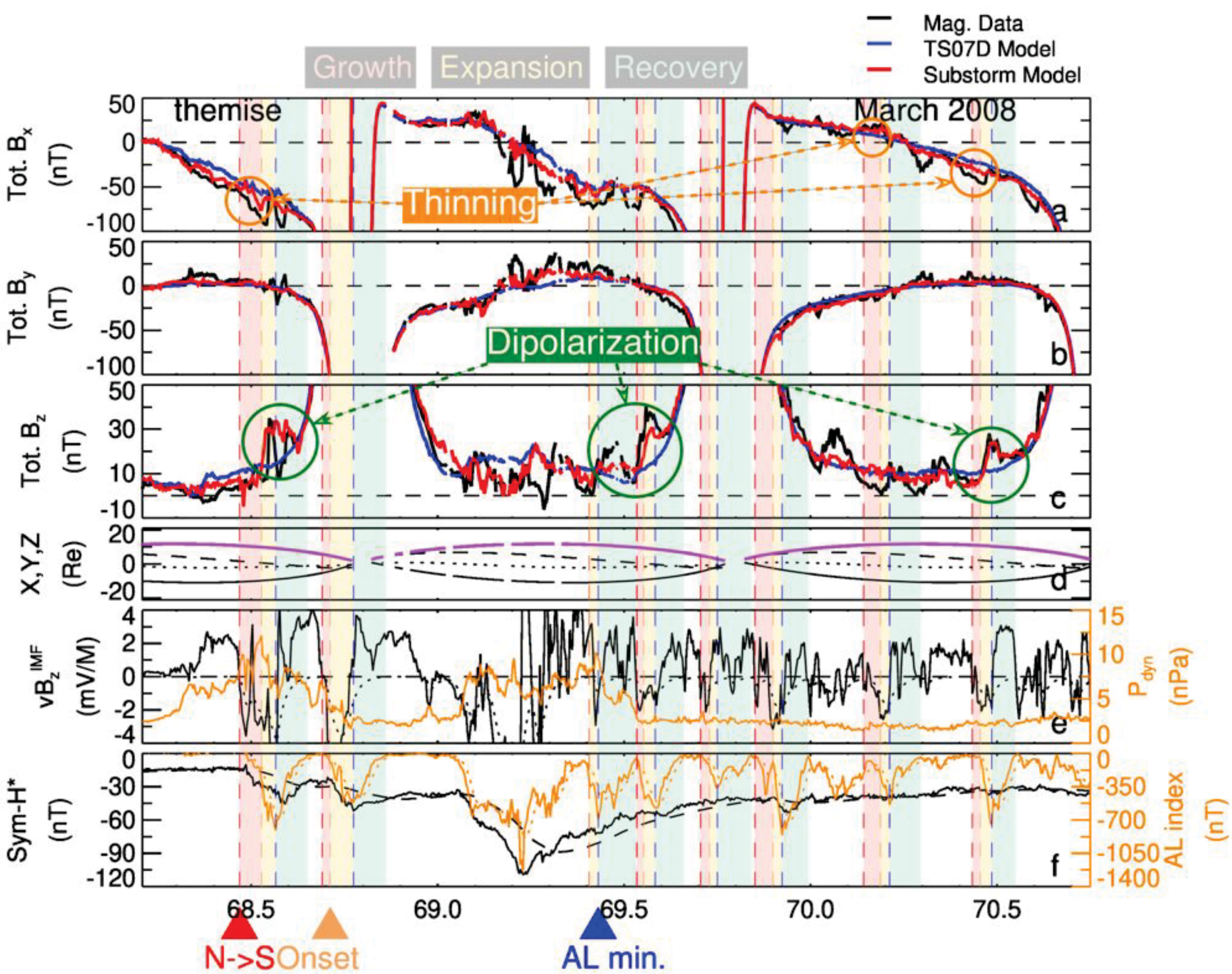

Mag. Data
TS07D Model
Substorm Model
Growth
Expansion
Recovery
themise
March 2008
Thinning
Dipolarization
Tot. B_x (nT)
Tot. B_y (nT)
Tot. B_z (nT)
X, Y, Z (Re)
vB_z^{IMF} (mV/M)
P_{dyn} (nPa)
Sym-H* (nT)
AL index (nT)
a
b
c
d
e
f
68.5
69.0
69.5
70.0
70.5
N->S
Onset
AL min.

F02.

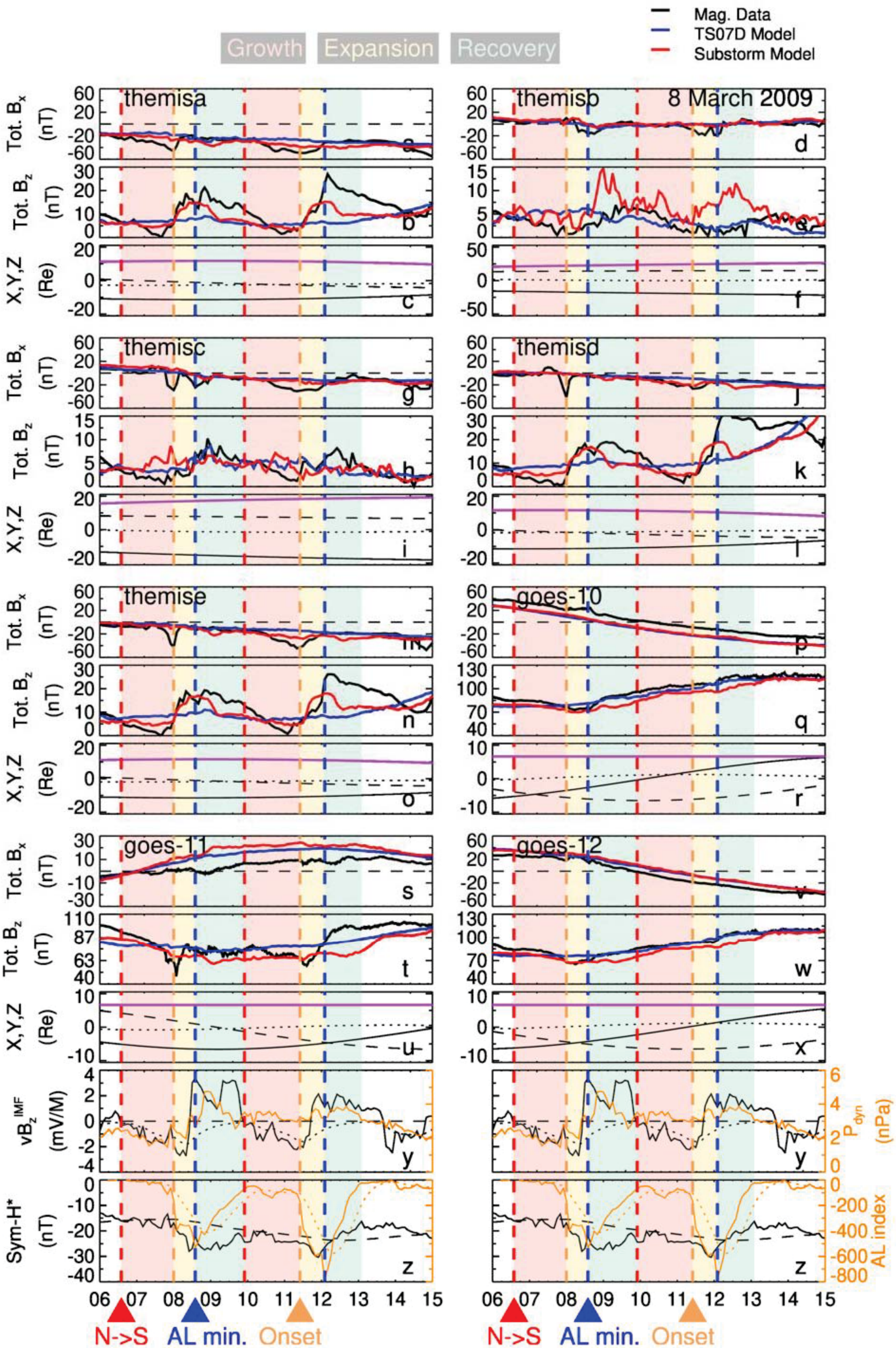

Mag. Data
TS07D Model
Substorm Model
Growth
Expansion
Recovery
themisa
themisb
8 March 2009
themisc
themisd
themise
goes-10
goes-11
goes-12
Tot. B$_x$ (nT)
Tot. B$_z$ (nT)
X,Y,Z (Re)
vB_z^{IMF} (mV/M)
P$_{dyn}$ (nPa)
Sym-H* (nT)
AL index (nT)
N->S
AL min.
Onset

F03.

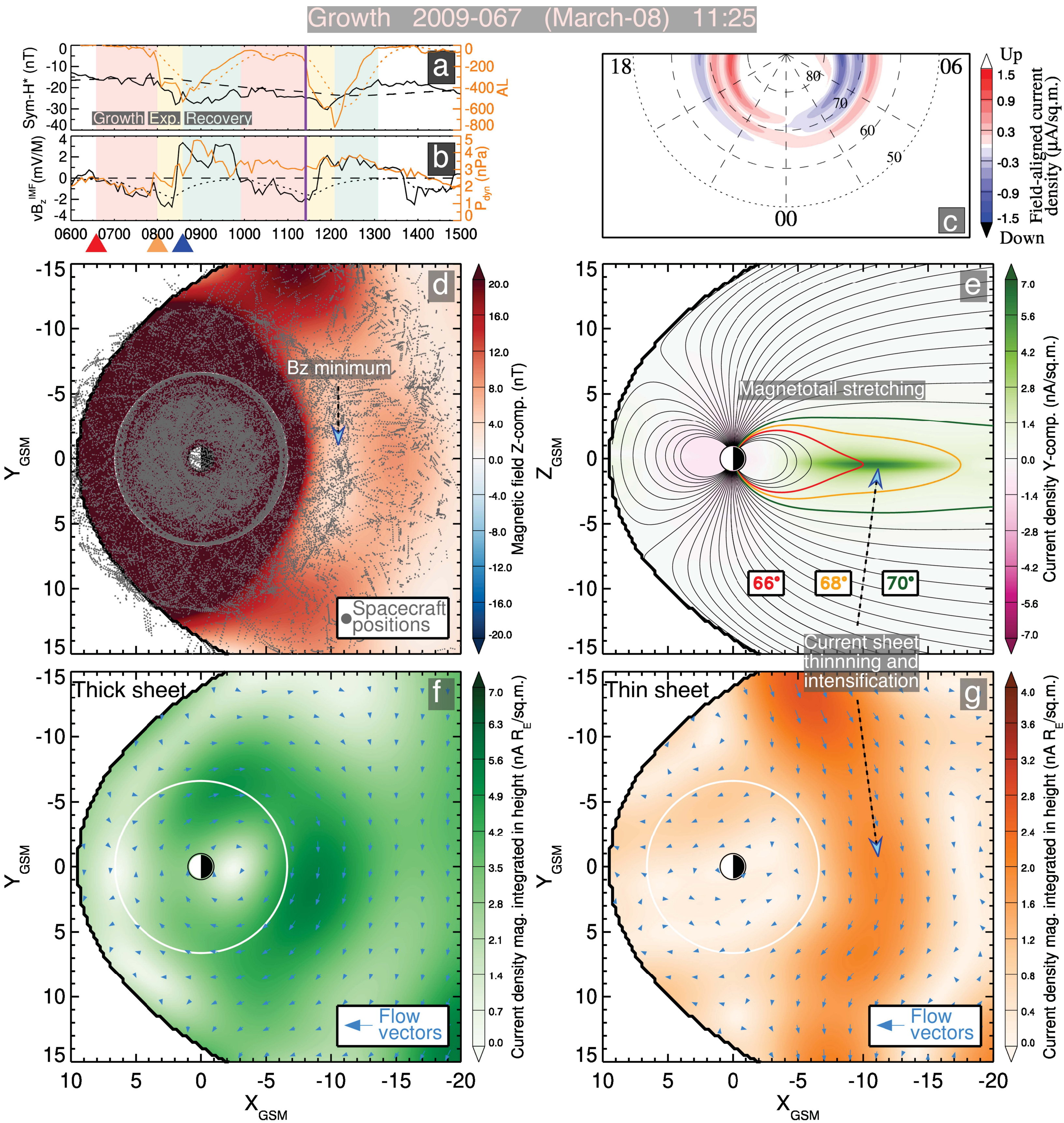

Growth 2009-067 (March-08) 11:25
Sym-H* (nT)
AL
Growth
Exp.
Recovery
a
vBz IMF (mV/M)
Pdyn (nPa)
b
0600 0700 0800 0900 1000 1100 1200 1300 1400 1500
18
06
00
80
70
60
50
c
Up
Down
Field-aligned current density (μA/sq.m.)
d
Bz minimum
Spacecraft positions
Magnetic field Z-comp. (nT)
YGSM
e
Magnetotail stretching
66°
68°
70°
Current sheet thinnning and intensification
Current density Y-comp. (nA/sq.m.)
ZGSM
f
Thick sheet
Flow vectors
Current density mag. integrated in height (nA RE/sq.m.)
g
Thin sheet
XGSM

F04.

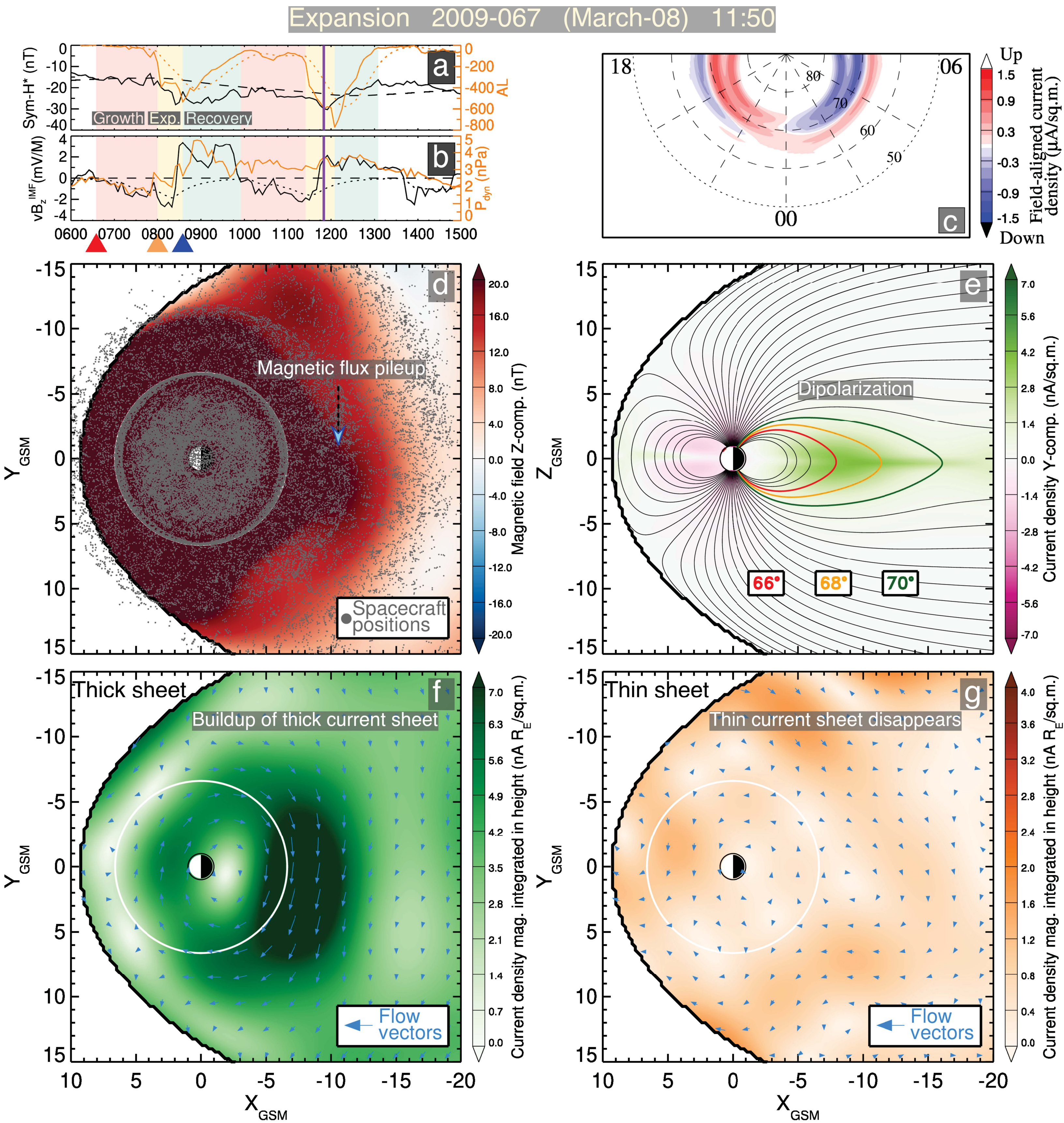

Expansion 2009-067 (March-08) 11:50
Sym-H* (nT)
AL
Growth
Exp.
Recovery
vBz IMF (mV/M)
Pdyn (nPa)
0600 0700 0800 0900 1000 1100 1200 1300 1400 1500
18
06
00
80
70
60
50
Up
Down
Field-aligned current density (μA/sq.m.)
Magnetic flux pileup
Spacecraft positions
Magnetic field Z-comp. (nT)
Dipolarization
66°
68°
70°
Current density Y-comp. (nA/sq.m.)
Thick sheet
Buildup of thick current sheet
Flow vectors
Current density mag. integrated in height (nA RE/sq.m.)
Thin sheet
Thin current sheet disappears
YGSM
ZGSM
XGSM
a
b
c
d
e
f
g

F05.

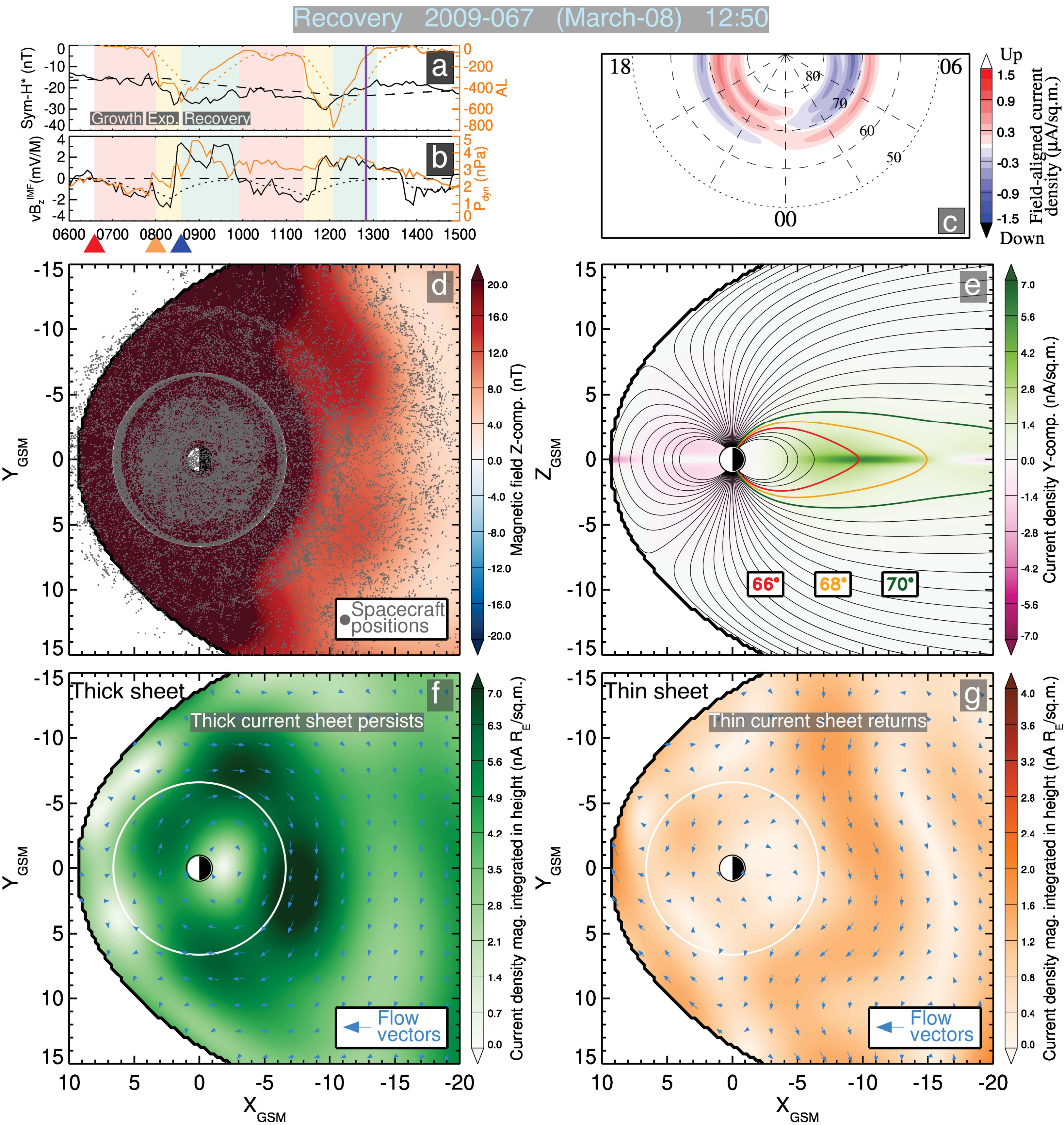

Recovery 2009-067 (March-08) 12:50
a
Sym-H* (nT)
AL
Growth
Exp.
Recovery
b
vBz IMF (mV/M)
Pdyn (nPa)
0600 0700 0800 0900 1000 1100 1200 1300 1400 1500
c
18
06
00
80
70
60
50
Up
Down
Field-aligned current density (μA/sq.m.)
d
YGSM
Magnetic field Z-comp. (nT)
Spacecraft positions
e
ZGSM
66°
68°
70°
Current density Y-comp. (nA/sq.m.)
f
Thick sheet
Thick current sheet persists
Flow vectors
Current density mag. integrated in height (nA RE/sq.m.)
g
Thin sheet
Thin current sheet returns
Flow vectors
XGSM

F06.

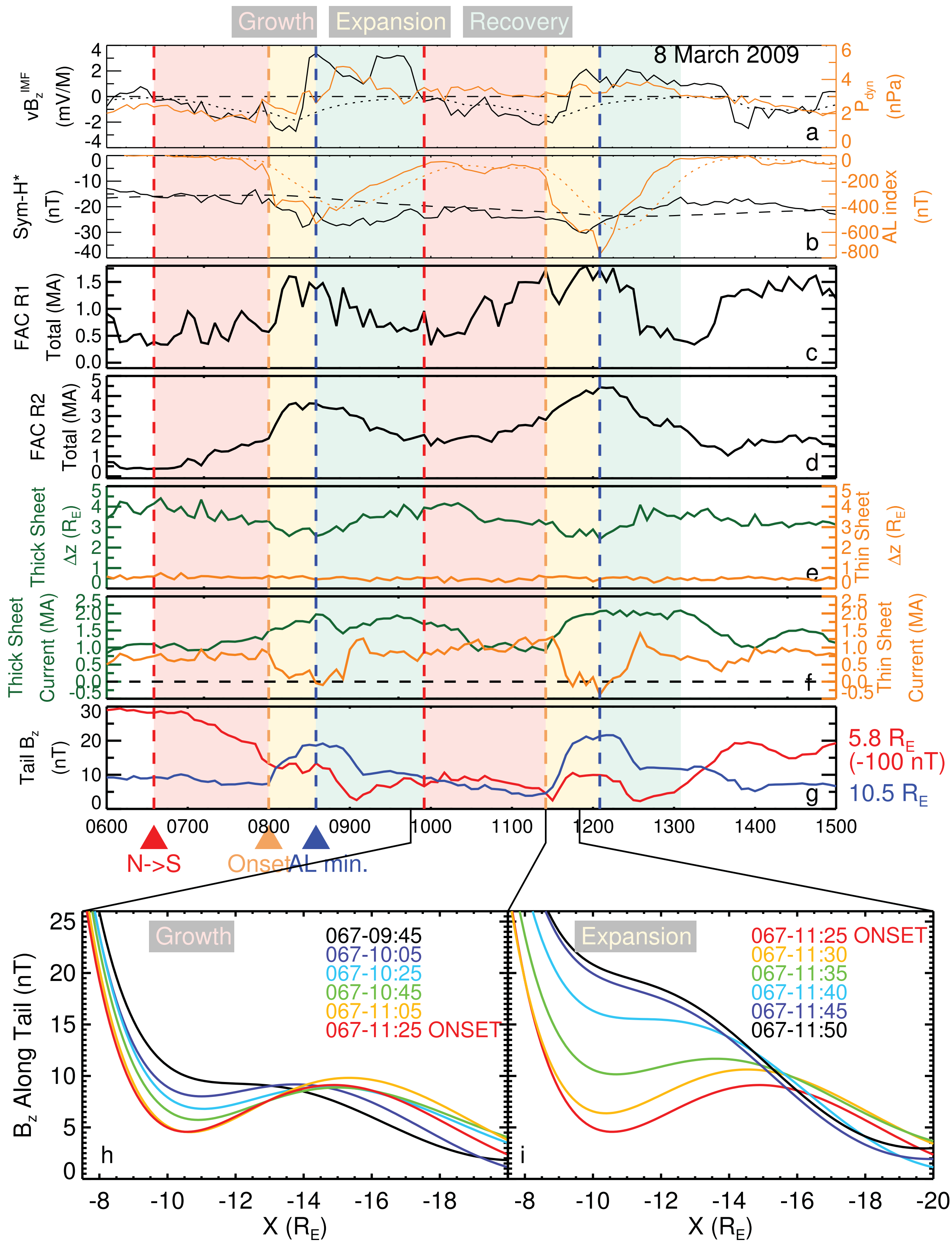

Growth
Expansion
Recovery
8 March 2009
vB_z^{IMF} (mV/M)
P_{dyn} (nPa)
Sym-H* (nT)
AL index (nT)
FAC R1 Total (MA)
FAC R2 Total (MA)
Thick Sheet Δz (R_E)
Thin Sheet Δz (R_E)
Thick Sheet Current (MA)
Thin Sheet Current (MA)
Tail B_z (nT)
5.8 R_E (-100 nT)
10.5 R_E
N->S
Onset
AL min.
B_z Along Tail (nT)
067-09:45
067-10:05
067-10:25
067-10:45
067-11:05
067-11:25 ONSET
067-11:30
067-11:35
067-11:40
067-11:45
067-11:50
X (R_E)

F07.

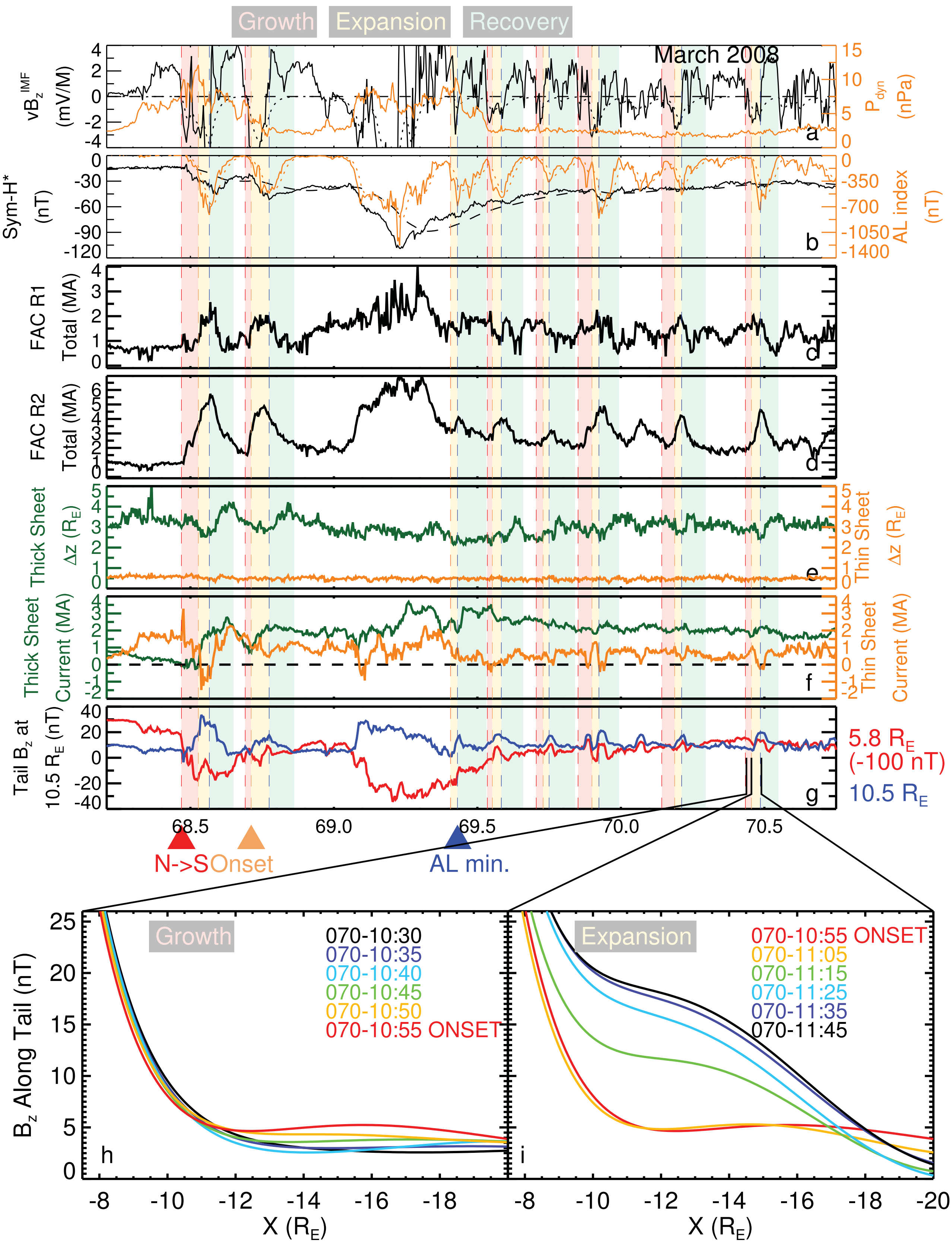

Growth
Expansion
Recovery
March 2008
vB_z^{IMF} (mV/M)
P_{dyn} (nPa)
a
Sym-H* (nT)
AL index (nT)
b
FAC R1 Total (MA)
c
FAC R2 Total (MA)
d
Thick Sheet Δz (R_E)
Thin Sheet Δz (R_E)
e
Thick Sheet Current (MA)
Thin Sheet Current (MA)
f
Tail B_z at 10.5 R_E (nT)
5.8 R_E (-100 nT)
10.5 R_E
g
68.5
69.0
69.5
70.0
70.5
N->S
Onset
AL min.
Growth
070-10:30
070-10:35
070-10:40
070-10:45
070-10:50
070-10:55 ONSET
B_z Along Tail (nT)
h
X (R_E)
Expansion
070-10:55 ONSET
070-11:05
070-11:15
070-11:25
070-11:35
070-11:45
i
X (R_E)

F08.

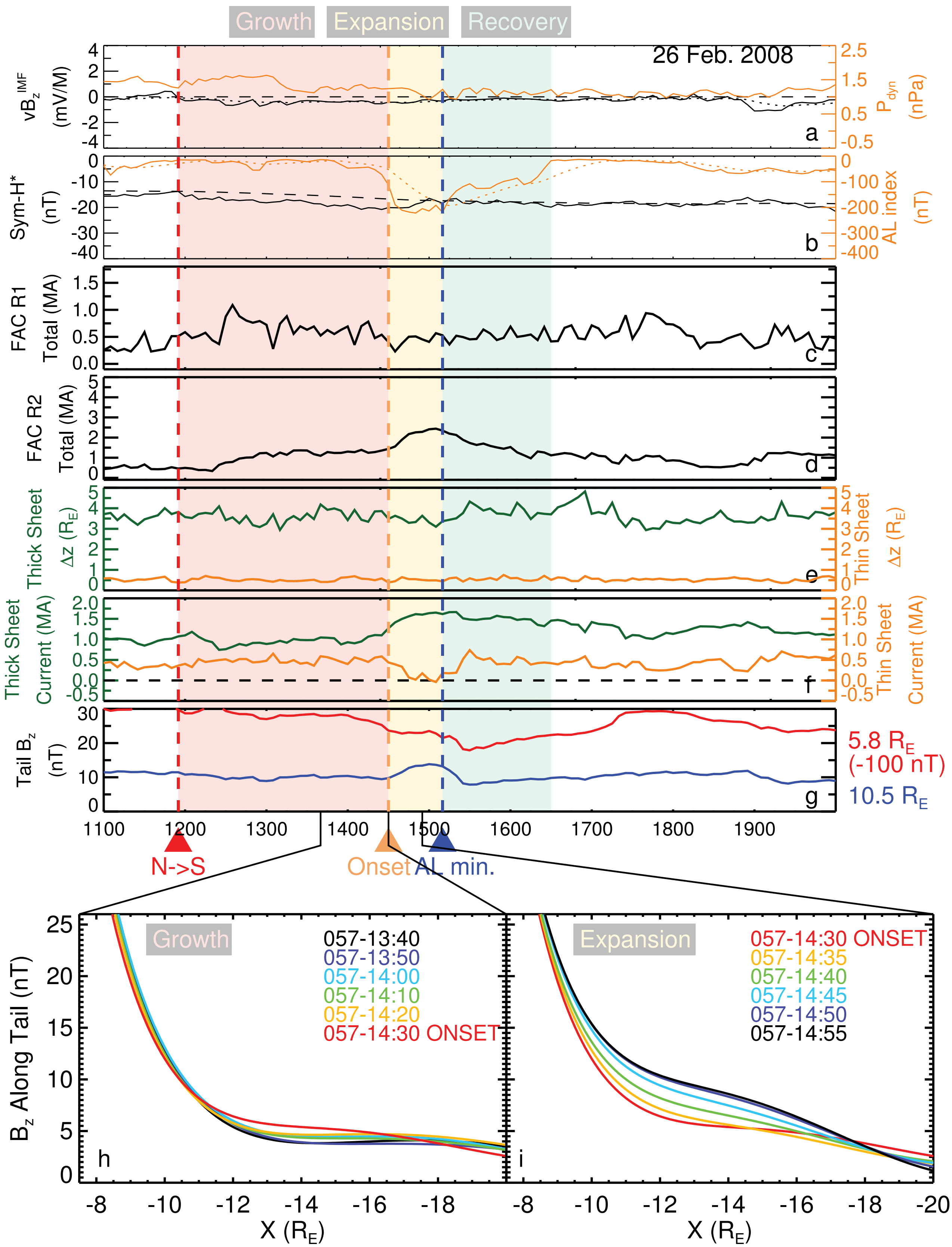

Growth
Expansion
Recovery
26 Feb. 2008
vBz IMF (mV/M)
Pdyn (nPa)
a
Sym-H* (nT)
AL index (nT)
b
FAC R1 Total (MA)
c
FAC R2 Total (MA)
d
Thick Sheet Δz (RE)
Thin Sheet Δz (RE)
e
Thick Sheet Current (MA)
Thin Sheet Current (MA)
f
Tail Bz (nT)
5.8 RE (-100 nT)
10.5 RE
g
N->S
Onset
AL min.
Bz Along Tail (nT)
Growth
057-13:40
057-13:50
057-14:00
057-14:10
057-14:20
057-14:30 ONSET
h
X (RE)
Expansion
057-14:30 ONSET
057-14:35
057-14:40
057-14:45
057-14:50
057-14:55
i
X (RE)

F09.

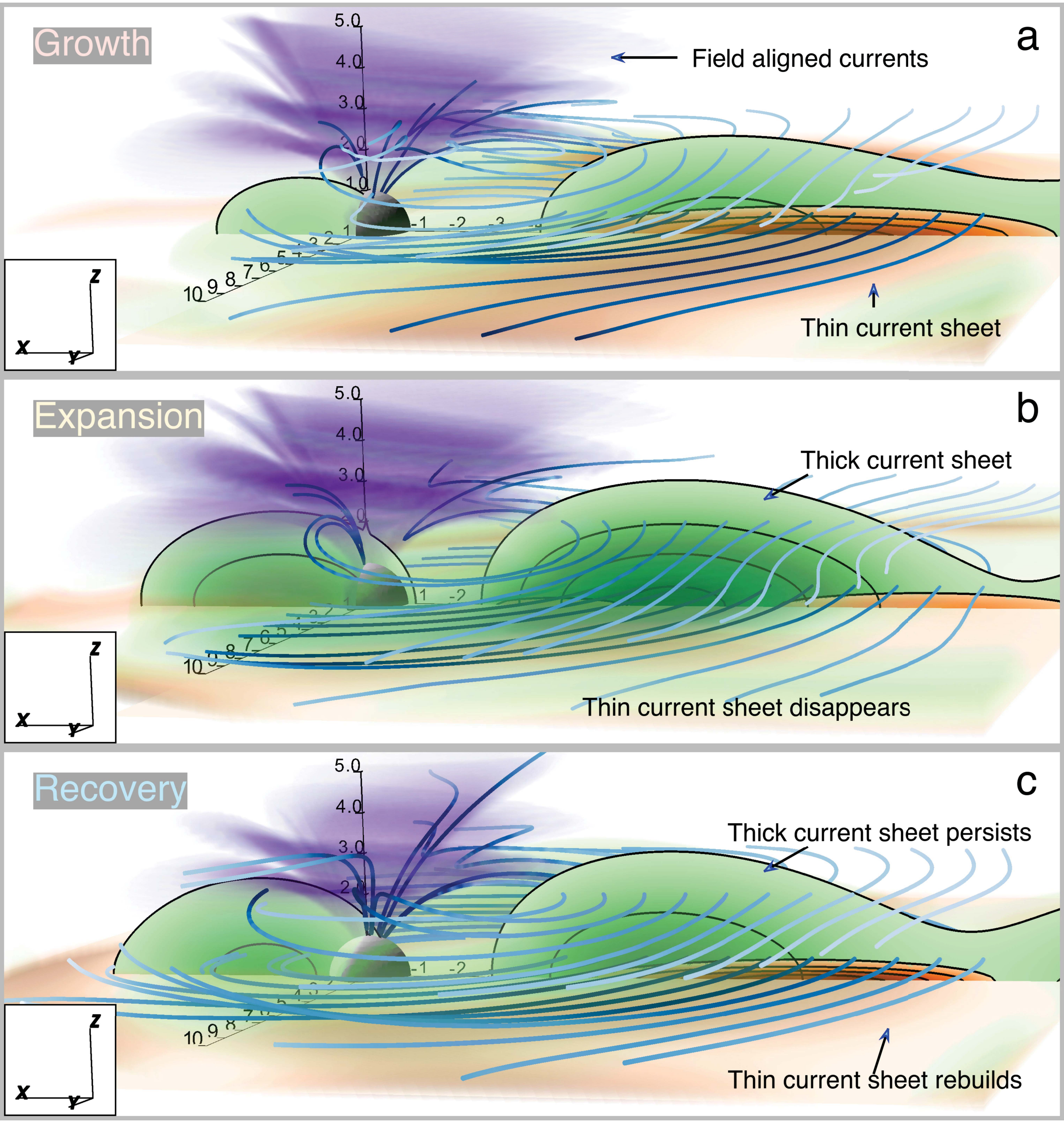
Growth
a
Field aligned currents
Thin current sheet
Expansion
b
Thick current sheet
Thin current sheet disappears
Recovery
c
Thick current sheet persists
Thin current sheet rebuilds

F01.

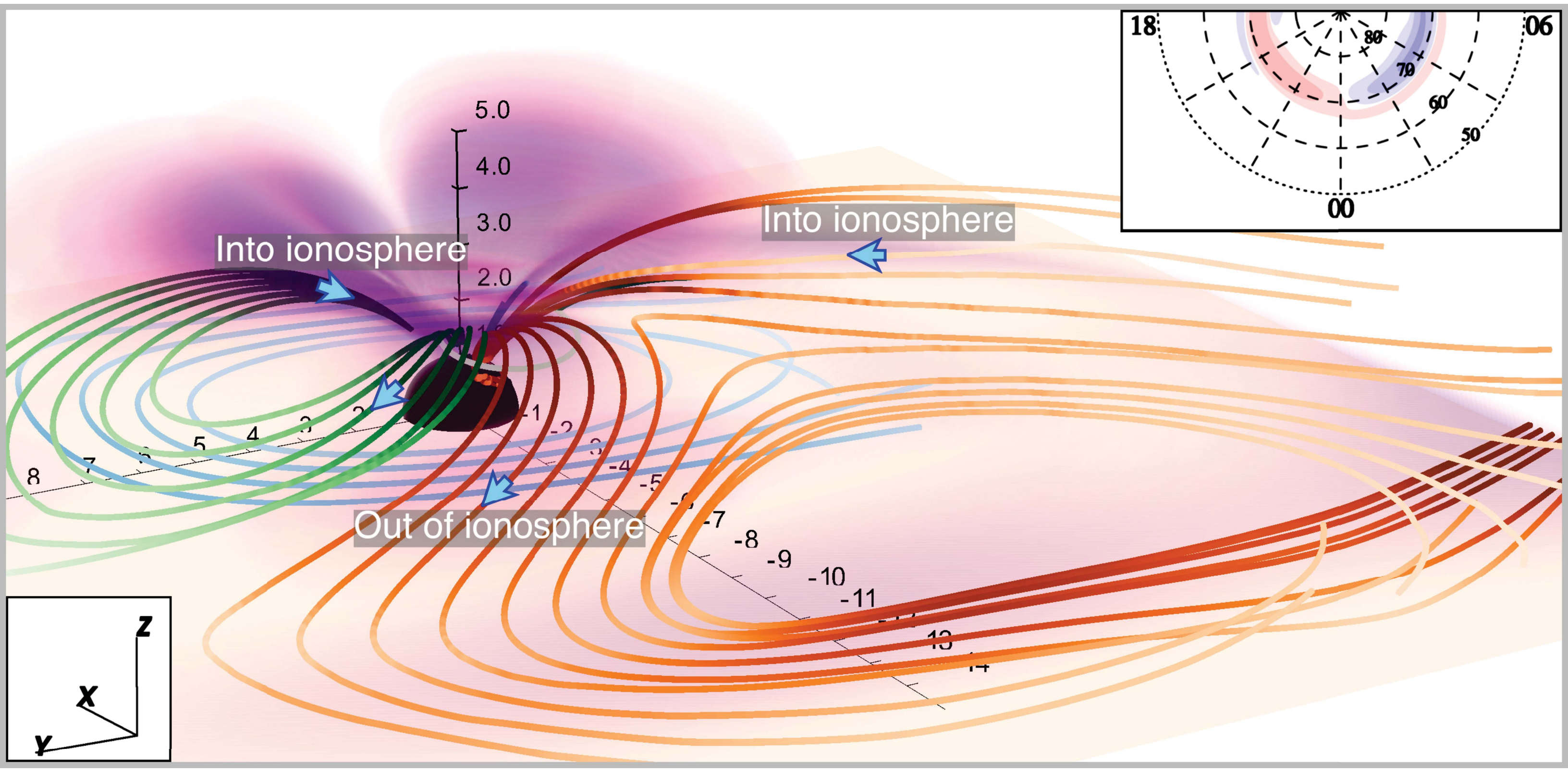

18
06
00
80
70
60
50
5.0
4.0
3.0
2.0
Into ionosphere
Into ionosphere
Out of ionosphere
8
7
5
4
-1
-5
-7
-8
-9
-10
-11
13
z
x
y

F11.

Substorm current wedge 2009-067 (March-08)